Journal of Optimization Theory and Applications
https://doi.org/10.1007/s10957-021-01892-1

Nonlinear Optimal Approach to Spacecraft Formation Flying Using Lorentz and Impulsive Actuation

Esmaeil Sharifi[1] · **Christopher J. Damaren**[1]

Received: 28 April 2020 / Accepted: 12 June 2021

Abstract
This paper proposes an optimal control design framework for hybrid nonlinear time-dependent dynamical systems involving an interacting mixture of continuous-time and discrete-time dynamics. Aiming to extend hybrid linear optimal control synthesis to nonlinear non-quadratic formulation, a hybrid version of the Hamilton–Jacobi–Bellman (HJB) equation with time-dependency is first presented. A hybrid computational framework, which alternates between continuous-time and discrete-time subsystems at an appropriate sequence of time instants, is then developed to solve the resultant set of the HJB equations in an interacting manner. The proposed control scheme is subsequently applied to spacecraft formation flying establishment with a hybrid source of actuation, namely Lorentz force and impulsive thrusting. By optimal combination of the Lorentz force and impulsive thrusting proposed in this paper, not only are the uncontrollability issues pertinent inherently to the Lorentz-actuated control systems effectively resolved, but use of both Lorentz and impulsive control inputs is also optimized. As a consequence, the expendable chemical fuels required to actuate thrusters are significantly reduced, thereby extending the duration of such space missions.

Keywords Spacecraft formation flight · Lorentz-augmented orbit · Hybrid nonlinear optimal time-varying control · Hamilton–Jacobi–Bellman equation · Galerkin/collocation-based approximation

Communicated by Mauro Pontani.

✉ Esmaeil Sharifi
esmaeil.sharifi@mail.utoronto.ca

Christopher J. Damaren
damaren@utias.utoronto.ca

[1] Spacecraft Dynamics and Control Laboratory, University of Toronto, Institute for Aerospace Studies, Toronto, ON M3H 5T6, Canada

Published online: 18 July 2021

1 Introduction

Spacecraft formation flight involving a collection of coordinated spacecraft flying in proximity has recently acquired increasing interests for many possible applications, including long baseline optical interferometry, stereographic imaging, atmospheric monitoring and control, synthetic apertures, and distinguishing spatial from temporal magnetospheric variations to name but a few [12, 13, 26]. Due to a wide range of advantages, from decreased cost and risk to increased flexibility and reliability along with enhanced performance, offered by formation flight, it has been identified as a key enabling technology for future space missions [7]. Spacecraft in formation establishment or reconfiguration are traditionally propelled by thrusters using chemical fuels onboard to perform relative orbital maneuvers. Duration of such space missions is therefore constrained by the amount of propellant available onboard. By extending the lifetime of a traditional space mission via alleviating the necessity for such expendable propellent, the propellantless propulsion systems have promisingly opened up new possibilities for future spacecraft missions. Instead of expending propellant, the spacecraft equipped with the propellantless propulsion technology exchange energy and momentum with the environment where they operate as a means of actuation [24].

The Lorentz force originating from the interaction between an electrostatically charged spacecraft traveling at a significant relative velocity and the Earth magnetic field can be used as electromagnetic propellantless propulsion to provide a useful thrust for near-Earth missions [14]. The basic concept underlying the Lorentz-based actuation mechanism is founded upon simple physical principles; a spacecraft utilizes electrical power to build up a net electrostatic charge on its body, and this very net charge causes an interaction between the geomagnetic field and the vehicle in the form of the Lorentz force [25]. The magnitude and direction of the resultant force are therefore defined by three factors: the size and polarity of the charge on the spacecraft, the relative velocity of the spacecraft with respect to the magnetic field, and the strength and direction of the magnetic field [25]. As a consequence, Lorentz propulsive actuation systems are used almost exclusively in Low Earth Orbits (LEOs) where the magnitude of the Earth magnetic field is sufficiently intense. This is due primarily to the fact that the magnitude of the geomagnetic field decreases as the inverse cube of the distance from the center of the Earth.

Prospects and challenges for using the Lorentz force as a means of propellantless propulsion for orbital maneuvering were first proposed in [13] and then in [22] along with preliminary designs, hardware development, and trajectory applications. The Lorentz propulsive actuation concept was subsequently applied to a wide variety of applications from absolute to relative orbital maneuvering; including new Earth-synchronous orbits [23], gravity-assist maneuvers [25], planetary capture or escape [1], propellantless station-keeping around small asteroids [9], flyby anomaly during low-altitude gravity-assist maneuvers around the Earth [2], and orbital inclination change [15] for absolute orbital applications, and spacecraft rendezvous [11, 16, 29] and formation flying [14, 16, 29] as to the application of the Lorentz force to relative orbital maneuvers.

Lorentz-augmented formation flight enjoys several advantages for near-Earth missions. First of all, the size of the induced Lorentz force is only limited by the charge-holding capacity and available power of the spacecraft [23]. Furthermore, whereas a propellant-based propulsion system can only deliver finite thrust for orbit control, Lorentz-based propelled spacecraft can offer the prospect of indefinite thrust [13]. On the other hand, as an inherent limitation, the direction of the Lorentz force is always constrained to lie orthogonal with respect to the velocity direction of the spacecraft and the direction of the magnetic field at the location of the spacecraft [24]. This is due essentially to the cross product between the relative velocity vector of the spacecraft and the Earth magnetic field vector from which the Lorentz force originates. Therefore, a formation flight control system which only utilizes the Lorentz force for actuation suffers always from a lack of full controllability. Moreover, Lorentz-based propulsion is impossible in some special cases; such scenario, for instance, arises when a polar satellite crosses the equator [13].

To resolve the abovementioned drawback, the Lorentz-augmented formation flight control system can be employed in conjunction with an additional active source of actuation. This paper proposes an interacting hybrid source of actuation, which alternates between the Lorentz force and impulsive thrusting in an optimal manner once a specific criterion is met, to address the foregoing uncontrollability issues. In this regard, the Lorentz force, as a continuous-time renewable source of actuation, is instantaneously switched to impulsive thrusts, as an active auxiliary source of propulsion, at an appropriate sequence of time instants to reliably provide the thrust required for formation establishment. Simultaneous use of Lorentz force and impulsive thrusting for formation flying establishment and reconfiguration was also studied in [19–21] by developing the so-called hybrid linear quadratic regulator (LQR) scheme to combine the two modes of actuation in an optimal manner. This paper aims to extend the tracking control synthesis proposed in [19–21] to nonlinear non-quadratic formulation. To this end, a hybrid version of the Hamilton–Jacobi–Bellman (HJB) equation with time-dependency is first formulated. A hybrid computational framework involving two numerical schemes, namely the Galerkin spectral method [8] and the spectral collocation technique [17] pertinent to continuous-time and discrete-time subsystems, is then developed to solve the resultant HJB equations in an interacting manner. An optimal control design framework is ultimately derived for hybrid nonlinear time-dependent dynamical systems involving an interacting mixture of continuous-time and discrete-time dynamics.

By optimal combination of the Lorentz force and impulsive thrusts proposed in this paper, not only are the uncontrollability issues involved inherently in the Lorentz-actuated control systems effectively resolved, but use of both Lorentz and impulsive control inputs is also optimized. This can lead to a considerable reduction in the expendable chemical fuels required to actuate the thrusters, which in turn extends the duration of such space missions. Furthermore, the feedback tracking controllers required to maintain bounded relative motion between spacecraft in formation are synthesized by considering the full nonlinear relative dynamics of the system. No linearization is involved, neither dynamic feedback linearization nor a priori linearization of the equations of motion. This is particularly useful for formation flight control systems which can involve large relative orbital maneuvers.

This paper is organized as follows. A novel optimal control design framework for hybrid nonlinear time-dependent dynamical systems is developed in Sect. 2. The equations of motion characterizing relative dynamics between multiple spacecraft in formation are then presented in Sect. 3. Section 4 serves to describe practical considerations for implementing the proposed control design framework. The hybrid control architecture developed in Sect. 2 is ultimately applied to spacecraft formation flight with a hybrid source of Lorentz and impulsive actuation in Sect. 5.

2 Hybrid Nonlinear Optimal Control

This section serves to develop an optimal control design framework for hybrid nonlinear time-dependent dynamical systems involving an interacting amalgam of continuous-time and discrete-time dynamics. The overall framework, in fact, provides the solid foundation for extending hybrid linear optimal control synthesis to nonlinear non-quadratic formulation. Consider a hybrid dynamical system modeled by equations of the form

$$\dot{\boldsymbol{x}}(t) = \boldsymbol{f}_{ct}(\boldsymbol{x},t) + \boldsymbol{g}_{ct}(\boldsymbol{x},t)\boldsymbol{u}_{ct}(t), \quad \boldsymbol{x}(t_0) = \boldsymbol{x}_0 \qquad t \neq t_k \tag{1}$$

$$\boldsymbol{x}_k^+ = \boldsymbol{f}_{ds}(\boldsymbol{x}_k^-,t) + \boldsymbol{g}_{ds}(\boldsymbol{x}_k^-,t)\boldsymbol{u}_{ds}(t) \quad t = t_k \tag{2}$$

where $t \geq 0$; $\boldsymbol{x} \in \mathcal{D} \subseteq \mathbb{R}^n$ is the state vector; $\mathcal{D}$ specifies an open set with $\mathbf{0} \in \mathcal{D}$ defined as the state space of interest; $\boldsymbol{f}_{ct} : \mathcal{D} \times \mathbb{R} \to \mathbb{R}^n$ is Lipschitz continuous on $\mathcal{D}$; $\boldsymbol{g}_{ct} : \mathcal{D} \times \mathbb{R} \to \mathbb{R}^{n \times m_{ct}}$; t_k denotes the time instants at which impulses are to be applied with $k \in \mathbb{Z}_{(t_0,t_\mathrm{f})} \triangleq \{k : t_0 < t_k < t_\mathrm{f}\}$; $\boldsymbol{x}_k^- \triangleq \boldsymbol{x}(t_k^-) \in \mathcal{D}$ and $\boldsymbol{x}_k^+ \triangleq \boldsymbol{x}(t_k^+) \in \mathcal{D}$ are, respectively, the state vector immediately before and after discrete-time dynamics are applied at $t = t_k$; $\boldsymbol{f}_{ds} : \mathcal{D} \times \mathbb{R} \to \mathbb{R}^n$ is continuous on $\mathcal{D}$; $\boldsymbol{g}_{ds} : \mathcal{D} \times \mathbb{R} \to \mathbb{R}^{n \times m_{ds}}$; and $(\boldsymbol{u}_{ct}, \boldsymbol{u}_{ds}) \in \boldsymbol{U}_{ct} \times \boldsymbol{U}_{ds} \subseteq \mathbb{R}^{m_{ct}} \times \mathbb{R}^{m_{ds}}$ denotes the hybrid control input for $t \in [t_0, t_\mathrm{f}]$ and $k \in \mathbb{Z}_{(t_0,t_\mathrm{f})}$. It is also assumed that $(\boldsymbol{u}_{ct}, \boldsymbol{u}_{ds})$ is restricted to the class of admissible control inputs $\mathcal{U} \triangleq \mathcal{U}_{ct} \times \mathcal{U}_{ds}$ consisting of measurable functions such that $(\boldsymbol{u}_{ct}, \boldsymbol{u}_{ds}) \in \boldsymbol{U}_{ct} \times \boldsymbol{U}_{ds}$, where the constraint set $\boldsymbol{U} \triangleq \boldsymbol{U}_{ct} \times \boldsymbol{U}_{ds}$ is given with $(\mathbf{0}, \mathbf{0}) \in \boldsymbol{U}_{ct} \times \boldsymbol{U}_{ds}$. The main objective is therefore to determine a hybrid nonlinear control input $(\boldsymbol{u}_{ct}, \boldsymbol{u}_{ds}) \in \boldsymbol{U}_{ct} \times \boldsymbol{U}_{ds}$, where $t \in [t_0, t_\mathrm{f}]$ and $k \in \mathbb{Z}_{(t_0,t_\mathrm{f})}$, such that the following hybrid performance index is minimized over all admissible control inputs $(\boldsymbol{u}_{ct}, \boldsymbol{u}_{ds}) \in \mathcal{U}_{ct} \times \mathcal{U}_{ds}$ [10]:

$$\mathcal{J}\big(\boldsymbol{x}_0, \boldsymbol{u}_{ct}(\cdot), \boldsymbol{u}_{ds}(\cdot), t_0\big) = \int_{t_0}^{t_\mathrm{f}} L_{ct}\big(\boldsymbol{x}(t), \boldsymbol{u}_{ct}(t), t\big)\mathrm{d}t + \sum_{k=1}^{\mathcal{K}} L_{ds}\big(\boldsymbol{x}(t_k), \boldsymbol{u}_{ds}(t_k), t_k\big) \tag{3}$$

where $L_{ct} : \mathcal{D} \times \boldsymbol{U}_{ct} \times \mathbb{R} \to \mathbb{R}$ and $L_{ds} : \mathcal{D} \times \boldsymbol{U}_{ds} \times \mathbb{R} \to \mathbb{R}$ denote, respectively, the continuous-time and discrete-time instantaneous cost functions, and $\mathcal{K}$ is the number of impulses applied during the operating time. Whereas the necessary and sufficient conditions for minimizing the hybrid performance index (3), given a hybrid control input $(\boldsymbol{u}_{ct}, \boldsymbol{u}_{ds})$, are obtained via a hybrid version of Bellman's principle of optimality ([10] Lemma 1), asymptotic stability of the hybrid nonlinear closed-loop system

can be guaranteed, assuming the dynamical properties of the system in question evolve *periodically*, by relating the hybrid performance index (3) to an underlying Lyapunov function in a specific way [10]. This Lyapunov function can be shown to serve as a solution of the hybrid HJB equation, thereby guaranteeing both optimality and asymptotic stability of the hybrid feedback control system (See [10, 18] for a detailed discussion).

With the main objective in view, the following hybrid version of the HJB equation involving a continuous-time partial differential equation with time-dependency and a discrete-time difference equation must be therefore solved in an interacting manner for $V(\boldsymbol{x}, t)$:

$$\partial V(\boldsymbol{x}\,,\,t)/\partial t + \min_{\boldsymbol{u}_{ct}\in\mathcal{U}_{ct}} \left\{\mathcal{H}_{ct}\big(\boldsymbol{x}, \boldsymbol{u}_{ct}, \partial V(\boldsymbol{x}, t)/\partial \boldsymbol{x}, t\big)\right\} = 0, \quad V(\boldsymbol{x}_{\mathrm{f}}\,,\,t_{\mathrm{f}}) = 0 \quad t \neq t_k \tag{4}$$

$$\min_{\boldsymbol{u}_{ds}\in\mathcal{U}_{ds}} \left\{\mathcal{H}_{ds}\big(\boldsymbol{x}, \boldsymbol{u}_{ds}, V(\boldsymbol{x}, t_k), t_k\big)\right\} = 0 \quad t = t_k \tag{5}$$

where $V : \mathcal{D}\times\mathbb{R} \to \mathbb{R}$ denotes a continuously differentiable positive-definite function known as *the value function* (the optimum value of the performance index), $\boldsymbol{x}_{\mathrm{f}} \triangleq \boldsymbol{x}(t_{\mathrm{f}})$, and $\mathcal{H}_{ct}$ and $\mathcal{H}_{ds}$ define, respectively, the Hamiltonians associated with the continuous-time and discrete-time dynamics as follows:

$$\mathcal{H}_{ct} \triangleq L_{ct}(\boldsymbol{x}, \boldsymbol{u}_{ct}, t) + (\partial V(\boldsymbol{x}, t)/\partial \boldsymbol{x})^{\mathrm{T}}\big(\boldsymbol{f}_{ct}(\boldsymbol{x}, t) + \boldsymbol{g}_{ct}(\boldsymbol{x}, t)\boldsymbol{u}_{ct}(t)\big) \tag{6}$$

$$\mathcal{H}_{ds} \triangleq L_{ds}(\boldsymbol{x}_k, \boldsymbol{u}_{ds}, t_k) + V(\boldsymbol{x}_k^+, t_k^+) - V(\boldsymbol{x}_k^-, t_k^-) \tag{7}$$

where $V(\boldsymbol{x}_k^+, t_k^+) = V(\boldsymbol{f}_{ds} + \boldsymbol{g}_{ds}\boldsymbol{u}_{ds}, t_k^+)$.

By defining non-quadratic instantaneous cost functions of the form $L_{ct}(\boldsymbol{x}, \boldsymbol{u}_{ct}, t) = l_{ct}(\boldsymbol{x}) + \|\boldsymbol{u}_{ct}(t)\|^2_{\boldsymbol{R}_{ct}}$ and $L_{ds}(\boldsymbol{x}_k^-, \boldsymbol{u}_{ds}, t_k) = l_{ds}(\boldsymbol{x}_k^-) + \|\boldsymbol{u}_{ds}(t_k)\|^2_{\boldsymbol{R}_{ds}}$ for the continuous-time and discrete-time subsystems, the hybrid nonlinear optimal control law in question can be consequently computed in terms of $V(\boldsymbol{x}, t)$ by minimizing (4) and (5), respectively, with respect to $\boldsymbol{u}_{ct}$ and $\boldsymbol{u}_{ds}$ as follows:

$$\boldsymbol{u}^*_{ct}(\boldsymbol{x}, t) = -\frac{1}{2}\boldsymbol{R}_{ct}^{-1}\boldsymbol{g}_{ct}^{\mathrm{T}}(\boldsymbol{x}, t)\frac{\partial V(\boldsymbol{x}, t)}{\partial \boldsymbol{x}} \quad t \neq t_k \tag{8}$$

$$\boldsymbol{u}^*_{ds,k} = -\frac{1}{2}\boldsymbol{R}_{ds}^{-1}\boldsymbol{g}_{ds}^{\mathrm{T}}\frac{\partial V(\boldsymbol{x}|_{\boldsymbol{x}=\boldsymbol{f}_{ds}+\boldsymbol{g}_{ds}\boldsymbol{u}^*_{ds,k}}, t_k^+)}{\partial \boldsymbol{x}} \quad t = t_k \tag{9}$$

where $\boldsymbol{u}_{ds,k} \triangleq \boldsymbol{u}_{ds}(\boldsymbol{x}_k, t_k)$, $l_{ct} : \mathcal{D} \to \mathbb{R}$ and $l_{ds} : \mathcal{D} \to \mathbb{R}$ denote, respectively, the continuous-time and discrete-time weighting functions acting on the system state, and $\boldsymbol{R}_{ct} = \boldsymbol{R}_{ct}^{\mathrm{T}} \in \mathbb{R}^{m_{ct}\times m_{ct}} > \boldsymbol{0}$ and $\boldsymbol{R}_{ds} = \boldsymbol{R}_{ds}^{\mathrm{T}} \in \mathbb{R}^{m_{ds}\times m_{ds}} > \boldsymbol{0}$ serve to panelize control inputs in appropriate subsystems. The resultant optimal control laws can be now substituted into (4) and (5) to formulate the following hybrid version of the HJB equations:

$$\frac{\partial V(\boldsymbol{x},t)}{\partial t}+\left(\frac{\partial V(\boldsymbol{x},t)}{\partial \boldsymbol{x}}\right)^{\mathrm{T}}\boldsymbol{f}_{ct}-\frac{1}{4}\left(\frac{\partial V(\boldsymbol{x},t)}{\partial \boldsymbol{x}}\right)^{\mathrm{T}}\boldsymbol{g}_{ct}\boldsymbol{R}_{ct}^{-1}\boldsymbol{g}_{ct}^{\mathrm{T}}\frac{\partial V(\boldsymbol{x},t)}{\partial \boldsymbol{x}}+l_{ct} = 0,\quad V(\boldsymbol{x}_{\mathrm{f}},t_{\mathrm{f}})=0 \quad t\neq t_k \tag{10}$$

$$V(\boldsymbol{\chi}_k^+,t_k^+)-V(\boldsymbol{x}_k^-,t_k^-)+\frac{1}{4}\left(\frac{\partial V(\boldsymbol{\chi}_k^+,t_k^+)}{\partial \boldsymbol{x}}\right)^{\mathrm{T}}\boldsymbol{g}_{ds}\boldsymbol{R}_{ds}^{-1}\boldsymbol{g}_{ds}^{\mathrm{T}}\left(\frac{\partial V(\boldsymbol{\chi}_k^+,t_k^+)}{\partial \boldsymbol{x}}\right)+l_{ds}=0 \quad t=t_k \tag{11}$$

where $\boldsymbol{\chi}_k^+ = \boldsymbol{f}_{ds}+\boldsymbol{g}_{ds}\boldsymbol{u}_{ds,k}^*$. The preceding set of the HJB equations must be therefore solved in an interacting manner to compute $V(\boldsymbol{x},t)$ in each subsystem to be fed to the foregoing optimal control laws represented by (8) and (9). Nevertheless, these equations are difficult to solve in general, thereby necessitating approximation techniques. To attain this objective, a hybrid computational framework, which alternates between the continuous-time and discrete-time subsystems at an appropriate sequence of time instants, is developed in the following subsections to approximates the value function in an interacting manner. The proposed hybrid scheme involves two numerical methods pertinent to each subsystem: the Galerkin spectral method, which approximates the value function between discrete-time events, and the spectral collocation method, which obtains an approximate solution for the discrete-time HJB equation at impulsive instants.

2.1 Numerical Solution to the Continuous-Time HJB Equation

Applying the Galerkin spectral method directly to the continuous-time portion of the hybrid HJB equation (10), a continuous-time set of differential equations is derived in this section to approximate the value function between discrete-time events. The basic idea underlying the Galerkin-based approximation is to assume that the solution of the continuous-time HJB equation can be expressed as an infinite sum of known basis functions. Furthermore, for the Galerkin spectral method to be applicable, the formulation must be placed in a suitable inner product space such that the projection is well-defined in terms of n-dimensional integrations [3]. The approximation is thus restricted to a closed and bounded set in $\mathcal{D}$, namely a compact set $\boldsymbol{\Omega}$, which defines the bounded domain of the state space of interest. To this end, it is first assumed that the value function can be discretized by an infinite series of prescribed state-dependent basis functions, which are continuous and defined everywhere on $\boldsymbol{\Omega}$, and unknown coefficients with time-dependency as follows:

$$V(\boldsymbol{x},\,t) := \sum_{j=1}^{\infty} c_j^*(t)\phi_j(\boldsymbol{x}) \tag{12}$$

Nevertheless, from a practical point of view, using an infinite number of terms for discretizing the value function is impossible; the approximation process for $V(\boldsymbol{x},\,t)$ is therefore carried one step further by considering a truncated version of the above-mentioned infinite series (i.e., the first N terms):

$$V_N(\boldsymbol{x}\,,\,t)\,:=\sum_{j=1}^{N} c_j^*(t)\phi_j(\boldsymbol{x}) = \boldsymbol{\Phi}_N^{\mathrm{T}}(\boldsymbol{x})\boldsymbol{C}_N^*(t) \tag{13}$$

where $\boldsymbol{\Phi}_N(\boldsymbol{x}) = \left[\phi_1(\boldsymbol{x})\,,\ldots\,,\,\phi_N(\boldsymbol{x})\right]^{\mathrm{T}}$ represents a prescribed state-dependent set of basis functions, $\boldsymbol{C}_N^*(t) = \left[c_1^*(t)\,,\ldots\,,\,c_N^*(t)\right]^{\mathrm{T}}$ specifies the corresponding collection of unknown time-dependent coefficients, and N denotes the number of basis elements, i.e., the order of approximation. The approximation sequence then proceeds with substituting (13) into (10), which, in turn, results in an error equation due primarily to approximating the value function with $V_N(\boldsymbol{x}\,,\,t)$. Employing the Galerkin spectral method, the unknown coefficients, $\left\{c_j^*(t)\right\}_{j=1}^{N}$, are determined such that the resultant error is minimized. To this end, the error equation is projected onto the same basis functions retained in the truncated series (i.e., the linear finite basis spanned by $\left\{\phi_j(\boldsymbol{x})\right\}_1^N$) and the outcome is set equal to zero in order to obtain N simultaneous equations for N unknowns:

$$\left\langle \mathrm{HJB}_{ct}\left(\sum_{j=1}^{N} c_j^*(t)\phi_j(\boldsymbol{x})\right),\,\boldsymbol{\Phi}_N(\boldsymbol{x})\right\rangle_{\boldsymbol{\Omega}} = \boldsymbol{0} \tag{14}$$

where the projection operator is the inner product $\langle(\cdot),\phi_i(\boldsymbol{x})\rangle_{\boldsymbol{\Omega}} \triangleq \int_{\boldsymbol{\Omega}}(\cdot)\phi_i(\boldsymbol{x})\mathrm{d}\boldsymbol{x}$ computed over a closed and bounded set, $\boldsymbol{\Omega}$. The preceding set of equations represents the Galerkin-based projection of the continuous-time HJB equation, (10), in a compact form, which can be expanded as follows:

$$\begin{aligned}&\langle\boldsymbol{\Phi}_N,\boldsymbol{\Phi}_N\rangle_{\boldsymbol{\Omega}}\dot{\boldsymbol{C}}_N^*(t) + \langle\mathbf{J}_{\boldsymbol{x}}(\boldsymbol{\Phi}_N)\boldsymbol{f}_{ct},\boldsymbol{\Phi}_N\rangle_{\boldsymbol{\Omega}}\boldsymbol{C}_N^*(t)\\ &\quad-\frac{1}{4}\left[\sum_{\kappa=1}^{N} c_\kappa^*(t)\left\langle\mathbf{J}_{\boldsymbol{x}}(\boldsymbol{\Phi}_N)\boldsymbol{g}_{ct}\boldsymbol{R}_{ct}^{-1}\boldsymbol{g}_{ct}^{T}\frac{\partial\phi_\kappa}{\partial\boldsymbol{x}},\boldsymbol{\Phi}_N\right\rangle_{\boldsymbol{\Omega}}\right]\boldsymbol{C}_N^*(t) + \langle l_{ct},\boldsymbol{\Phi}_N\rangle_{\boldsymbol{\Omega}} = \boldsymbol{0}\end{aligned} \tag{15}$$

where $\mathbf{J}_{\boldsymbol{x}}$ denotes the Jacobian operator (matrix) with respect to $\boldsymbol{x}$. The following set of nonlinear ordinary differential equations termed *the continuous-time optimal control gain equations* needs therefore to be integrated backward in time, beginning with the boundary conditions at the terminal time $\boldsymbol{C}_N^*(t_{\mathrm{f}})$, in order to compute $\boldsymbol{C}_N^*(t)$ between impulsive instants:

$$\dot{\boldsymbol{C}}_N^*(t) + \mathcal{Q}(c^*(t),t)\boldsymbol{C}_N^*(t) + \boldsymbol{d} = \boldsymbol{0}\quad,\quad \boldsymbol{C}_N^*(t_{\mathrm{f}}) = \boldsymbol{0} \tag{16}$$

where the equations are assumed to have no escape in finite-time, and

$$\begin{aligned}\mathcal{M}(c^*(t),t) &= \sum_{\kappa=1}^{N} c_\kappa^*(t)\left\langle\mathbf{J}_{\boldsymbol{x}}(\boldsymbol{\Phi}_N)\boldsymbol{g}_{ct}\boldsymbol{R}_{ct}^{-1}\boldsymbol{g}_{ct}^{\mathrm{T}}\frac{\partial\phi_\kappa}{\partial\boldsymbol{x}},\boldsymbol{\Phi}_N\right\rangle_{\boldsymbol{\Omega}}\\ \mathcal{Q}(c^*(t),t) &= \langle\boldsymbol{\Phi}_N,\boldsymbol{\Phi}_N\rangle_{\boldsymbol{\Omega}}^{-1}\left[\langle\mathbf{J}_{\boldsymbol{x}}(\boldsymbol{\Phi}_N)\boldsymbol{f}_{ct},\boldsymbol{\Phi}_N\rangle_{\boldsymbol{\Omega}} - \frac{1}{4}\mathcal{M}(c^*(t),t)\right]\\ \boldsymbol{d} &= \langle\boldsymbol{\Phi}_N,\boldsymbol{\Phi}_N\rangle_{\boldsymbol{\Omega}}^{-1}\langle l_{ct},\boldsymbol{\Phi}_N\rangle_{\boldsymbol{\Omega}}\end{aligned} \tag{17}$$

Once the time-varying optimal control gains, $\boldsymbol{C}_N^*(t)$, are computed via backward integration of (16), the continuous-time optimal control law can be obtained by:

$$\boldsymbol{u}_{ct}^*(\boldsymbol{x}\,,\,t) = -\frac{1}{2}\boldsymbol{R}_{ct}^{-1}\boldsymbol{g}_{ct}^{\mathrm{T}}(\boldsymbol{x}\,,\,t)\mathbf{J}_{\boldsymbol{x}}^{\mathrm{T}}\big(\boldsymbol{\Phi}_N(\boldsymbol{x})\big)\boldsymbol{C}_N^*(t) \tag{18}$$

2.2 Numerical Solution to the Discrete-Time HJB Equation

With the continuous-time optimal control gain equations thus derived, the spectral collocation method is utilized in this section to develop a set of algebraic equations with the purpose of computing the value function in the discrete-time subsystem when impulses are applied at $t = t_k$. The main idea behind the spectral collocation technique is to project (11) onto a discrete basis at each impulsive instant to produce as many equations as required for the unknowns. This is analogous to the Galerkin spectral method wherein the error equation resulted from approximating the value function is projected onto a truncated set of basis elements to obtain N simultaneous equations for N unknowns.

With the preceding objective in view, a truncated version of the discretized value function, (13), is substituted into (11) to formulate the following set of algebraic equations at each impulsive instant:

$$\begin{aligned}&\boldsymbol{\Phi}_N^{\mathrm{T}}(\boldsymbol{x})\Big|_{\boldsymbol{x}=\boldsymbol{f}_{ds}+\boldsymbol{g}_{ds}\boldsymbol{u}_{ds,k}^*}\boldsymbol{C}_N^*(t_k^+) - \boldsymbol{\Phi}_N^{\mathrm{T}}(\boldsymbol{x})\Big|_{\boldsymbol{x}=\boldsymbol{x}_k^-}\boldsymbol{C}_N^*(t_k^-) + l_{ds}(\boldsymbol{x}_k^-)\\ &\quad+\frac{1}{4}\left[\mathbf{J}_{\boldsymbol{x}}^{\mathrm{T}}\big(\boldsymbol{\Phi}_N(\boldsymbol{x})\big)\Big|_{\boldsymbol{x}=\boldsymbol{f}_{ds}+\boldsymbol{g}_{ds}\boldsymbol{u}_{ds,k}^*}\boldsymbol{C}_N^*(t_k^+)\right]^{\mathrm{T}}\boldsymbol{g}_{ds}\boldsymbol{R}_{ds}^{-1}\boldsymbol{g}_{ds}^{\mathrm{T}}\left[\mathbf{J}_{\boldsymbol{x}}^{\mathrm{T}}\big(\boldsymbol{\Phi}_N(\boldsymbol{x})\big)\Big|_{\boldsymbol{x}=\boldsymbol{f}_{ds}+\boldsymbol{g}_{ds}\boldsymbol{u}_{ds,k}^*}\boldsymbol{C}_N^*(t_k^+)\right] = 0\end{aligned} \tag{19}$$

Having the knowledge of $\boldsymbol{C}_N^*(t_k^+)$ available from the backward integration of (16), $\boldsymbol{C}_N^*(t_k^-)$ can be thus computed through the above set of equations. However, the state knowledge at $t = t_k^+$, $\boldsymbol{x}_k^+$, is required to reach this objective, which, in consequence, provides a new challenge. Since $\boldsymbol{x}_k^+$ resets the system state as a function of $\boldsymbol{x}_k^-$ and $\boldsymbol{u}_{ds,k}^*$ at $t = t_k$ in accordance with the discrete-time dynamics (2), there are two main avenues of further formulation to compute $\boldsymbol{C}_N^*(t_k^-)$ through (19) at each impulse. The methodology proposed in this paper to address this issue consists of three steps as follows.

In the first step, the discrete-time optimal control at $t = t_k$, $\boldsymbol{u}_{ds,k}^*$, is approximated by substituting the truncated version of the discretized value function, (13), into (9) as follows:

$$\boldsymbol{u}_{ds,k}^* = -\frac{1}{2}\boldsymbol{R}_{ds}^{-1}\boldsymbol{g}_{ds}^{\mathrm{T}}(\boldsymbol{x}_k^-, t_k)\sum_{j=1}^{N} c_j^*(t_k^+)\left.\frac{\partial\phi_j(\boldsymbol{x})}{\partial\boldsymbol{x}}\right|_{\boldsymbol{x}=\boldsymbol{f}_{ds}(\boldsymbol{x}_k^-,t_k)+\boldsymbol{g}_{ds}(\boldsymbol{x}_k^-,t_k)\boldsymbol{u}_{ds,k}^*} \tag{20}$$

To proceed further, the following set of equations in terms of $\boldsymbol{x}_k^-$ and $\boldsymbol{u}_{ds,k}^*$, with known quantities $\left\{ c_j^*(t_k^+) \right\}_{j=1}^N$, is then defined at $t = t_k$ by rearranging (20):

$$\mathcal{F}_k(\boldsymbol{x}_k^-, \boldsymbol{u}_{ds,k}^*) = 2\boldsymbol{R}_{ds}\boldsymbol{u}_{ds,k}^* + \boldsymbol{g}_{ds}^{\mathrm{T}}(\boldsymbol{x}_k^-, t_k) \sum_{j=1}^{N} c_j^*(t_k^+) \left. \frac{\partial \phi_j(\boldsymbol{x})}{\partial \boldsymbol{x}} \right|_{\boldsymbol{x} = \boldsymbol{f}_{ds}(\boldsymbol{x}_k^-, t_k) + \boldsymbol{g}_{ds}(\boldsymbol{x}_k^-, t_k)\boldsymbol{u}_{ds,k}^*} = \boldsymbol{0} \tag{21}$$

In the second step, $\boldsymbol{x}_k^-$ is collocated with a suitable set of points, $\bar{\boldsymbol{x}} = \underset{m}{\mathrm{row}} \left\{ \bar{\boldsymbol{x}}_m \right\}$ where $\bar{\boldsymbol{x}}_m \in \mathbb{R}^n$ and $m = 1, \ldots, N$, at each impulsive instant. With the state knowledge at $t = t_k^-$, $\boldsymbol{x}_k^-$, thus determined, (21) can be therefore converted into the following series of equations at $t = t_k$ involving one single unknown, $\boldsymbol{u}_{ds,k,m}^*$, which, in fact, represent a projected version of (21) on m^{th} column of a discrete basis spanned by $\bar{\boldsymbol{x}}$:

$$\mathcal{F}_{k,m}(\boldsymbol{u}_{ds,k,m}^*) = 2\boldsymbol{R}_{ds}\boldsymbol{u}_{ds,k,m}^* + \boldsymbol{g}_{ds}^{\mathrm{T}}(\bar{\boldsymbol{x}}_m, t_k) \sum_{j=1}^{N} c_j^*(t_k^+) \left. \frac{\partial \phi_j(\boldsymbol{x})}{\partial \boldsymbol{x}} \right|_{\boldsymbol{x} = \boldsymbol{f}_{ds}(\bar{\boldsymbol{x}}_m, t_k) + \boldsymbol{g}_{ds}(\bar{\boldsymbol{x}}_m, t_k)\boldsymbol{u}_{ds,k,m}^*} = \boldsymbol{0} \tag{22}$$

where $\boldsymbol{u}_{ds,k,m}^* \triangleq \boldsymbol{u}_{ds}^*(\bar{\boldsymbol{x}}_m, t_k)$ and $\mathcal{F}_k = \underset{m}{\mathrm{row}} \left\{ \mathcal{F}_{k,m} \right\} = \left[\mathcal{F}_{k,1}, \ \ldots, \ \mathcal{F}_{k,N} \right]_{m_{ds} \times N}$.

Proceeding to the last step in the proposed methodology, an appropriate numerical scheme is therefore employed to solve the preceding nonlinear set of algebraic equations for $\boldsymbol{u}_{ds,k,m}^*$. To this end, Newton's method [17], as an efficient iterative numerical scheme with quick convergence, is utilized to solve $\mathcal{F}_{k,m}(\boldsymbol{u}_{ds,k,m}^*) = \boldsymbol{0}$ for $\boldsymbol{u}_{ds,k,m}^{*(i+1)}$, beginning with $\boldsymbol{u}_{ds,k,m}^{*(i)}$, iteratively:

$$\boldsymbol{u}_{ds,k,m}^{*(i+1)} = \boldsymbol{u}_{ds,k,m}^{*(i)} - \left(\frac{\partial \mathcal{F}_{k,m}(\boldsymbol{u}_{ds,k,m}^{*(i)})}{\partial \boldsymbol{u}_{ds,k,m}^{*\mathrm{T}}} \right)^{-1} \mathcal{F}_{k,m}(\boldsymbol{u}_{ds,k,m}^{*(i)}) \tag{23}$$

In this regard, (22) is first injected into (23) and the chain rule is then used to formulate the following set of equations to be solved iteratively for $\boldsymbol{u}_{ds,k,m}^*$:

$$\begin{aligned} \boldsymbol{u}_{ds,k,m}^{*(i+1)} = \boldsymbol{u}_{ds,k,m}^{*(i)} - & \left(2\boldsymbol{R}_{ds} + \boldsymbol{g}_{ds}^{\mathrm{T}} \sum_{j=1}^{N} c_j^*(t_k^+) \mathbf{H}_{\boldsymbol{x}} \left(\phi_j(\boldsymbol{x}) \right) \Big|_{\boldsymbol{x} = \boldsymbol{\chi}_{k,m}^+} \boldsymbol{g}_{ds} \right)^{-1} \\ & \left(2\boldsymbol{R}_{ds}\boldsymbol{u}_{ds,k,m}^{*(i)} + \boldsymbol{g}_{ds}^{\mathrm{T}} \mathbf{J}_{\boldsymbol{x}}^{\mathrm{T}} \left(\boldsymbol{\Phi}_N(\boldsymbol{x}) \right) \Big|_{\boldsymbol{x} = \boldsymbol{\chi}_{k,m}^+} \boldsymbol{C}_N^*(t_k^+) \right) \end{aligned} \tag{24}$$

where $\boldsymbol{\chi}_{k,m}^+ = \boldsymbol{f}_{ds}(\bar{\boldsymbol{x}}_m, t_k) + \boldsymbol{g}_{ds}(\bar{\boldsymbol{x}}_m, t_k)\boldsymbol{u}_{ds,k,m}^{*(i)}$ and $\mathbf{H}_{\boldsymbol{x}}$ denotes the Hessian matrix with respect to $\boldsymbol{x}$.

Initializing (24) with a suitable choice of $\boldsymbol{u}_{ds,k,m}^{*(0)}$ (for instance, $\boldsymbol{u}_{ds,k,m}^{*(0)} = \boldsymbol{0}$, which usually work well), the discrete-time optimal control at $t = t_k$ corresponding to each $\bar{\boldsymbol{x}}_m$, $\boldsymbol{u}_{ds,k,m}^*$, can be therefore computed for $m = 1, \ldots, N$ to construct an array of the form $\boldsymbol{u}_{ds,k}^* = \underset{m}{\mathrm{row}} \left\{ \boldsymbol{u}_{ds,k,m}^* \right\} = \left[\boldsymbol{u}_{ds,k,1}^*, \ \ldots, \ \boldsymbol{u}_{ds,k,N}^* \right]_{m_{ds} \times N}$.

The required tools are now in place to solve (19) for $\boldsymbol{C}_N^*(t_k^-)$ at each impulse. To this end, the spectral collocation method is employed at this juncture in the

development to project (19) onto a discrete basis represented by $\bar{\boldsymbol{x}} = \underset{m}{\text{row}}\left\{\bar{\boldsymbol{x}}_m\right\} = \left[\bar{\boldsymbol{x}}_1, \ldots, \bar{\boldsymbol{x}}_N\right]_{n\times N}$, where $\bar{\boldsymbol{x}}_m \in \mathbb{R}^n$, at each impulsive instant to obtain N simultaneous algebraic equations for N unknowns $\left\{c_j^*(t_k^-)\right\}_{j=1}^N$. Utilizing the spectral collocation method and $\boldsymbol{u}_{ds,k,m}^*$ computed from (24) simultaneously, (19) is ultimately converted into the following set of algebraic equations termed *the discrete-time optimal control gain equations* to be solved for $\boldsymbol{C}_N^*(t_k^-)$ at each impulsive instant as follows:

$$\boldsymbol{C}_N^*(t_k^-) = \left(\boldsymbol{\Psi}_k(\bar{\boldsymbol{x}})\right)^{-1}\left[\boldsymbol{W}_k(\bar{\boldsymbol{x}}, t_k) + \mathbf{Z}_k(\bar{\boldsymbol{x}}, t_k)\boldsymbol{C}_N^*(t_k^+)\right] \tag{25}$$

where

$$\begin{aligned}
\boldsymbol{\Upsilon}_k(\bar{\boldsymbol{x}}_m, t_k) &= \mathbf{J}_{\boldsymbol{x}}^{\mathrm{T}}\left(\boldsymbol{\Phi}_N(\boldsymbol{x})\right)\Big|_{\boldsymbol{x}=\boldsymbol{f}_{ds}(\bar{\boldsymbol{x}}_m,t_k)+\boldsymbol{g}_{ds}(\bar{\boldsymbol{x}}_m,t_k)\boldsymbol{u}_{ds,k,m}^*}\boldsymbol{C}_N^*(t_k^+)\\
\boldsymbol{W}_k(\bar{\boldsymbol{x}}, t_k) &= \underset{m}{\text{column}}\left\{l_{ds}(\bar{\boldsymbol{x}}_m) + \frac{1}{4}\left(\boldsymbol{\Upsilon}_k^{\mathrm{T}}(\bar{\boldsymbol{x}}_m, t_k)\boldsymbol{g}_{ds}(\bar{\boldsymbol{x}}_m, t_k)\boldsymbol{R}_{ds}^{-1}\boldsymbol{g}_{ds}^{\mathrm{T}}(\bar{\boldsymbol{x}}_m, t_k)\boldsymbol{\Upsilon}_k(\bar{\boldsymbol{x}}_m, t_k)\right)\right\}\\
&= \begin{bmatrix} l_{ds}(\bar{\boldsymbol{x}}_1) + \frac{1}{4}\left(\boldsymbol{\Upsilon}^{\mathrm{T}}(\bar{\boldsymbol{x}}_1, t_k)\boldsymbol{g}_{ds}(\bar{\boldsymbol{x}}_1, t_k)\boldsymbol{R}_{ds}^{-1}\boldsymbol{g}_{ds}^{\mathrm{T}}(\bar{\boldsymbol{x}}_1, t_k)\boldsymbol{\Upsilon}(\bar{\boldsymbol{x}}_1, t_k)\right) \\ \vdots \\ l_{ds}(\bar{\boldsymbol{x}}_N) + \frac{1}{4}\left(\boldsymbol{\Upsilon}^{\mathrm{T}}(\bar{\boldsymbol{x}}_N, t_k)\boldsymbol{g}_{ds}(\bar{\boldsymbol{x}}_N, t_k)\boldsymbol{R}_{ds}^{-1}\boldsymbol{g}_{ds}^{\mathrm{T}}(\bar{\boldsymbol{x}}_N, t_k)\boldsymbol{\Upsilon}(\bar{\boldsymbol{x}}_N, t_k)\right)\end{bmatrix}_{N\times 1}\\
\boldsymbol{\Psi}_k(\bar{\boldsymbol{x}}) &= \underset{m,j}{\text{matrix}}\left\{\phi_j(\boldsymbol{x})\Big|_{\boldsymbol{x}=\bar{\boldsymbol{x}}_m}\right\}\\
&= \begin{bmatrix} \phi_1(\boldsymbol{x})\big|_{\boldsymbol{x}=\bar{\boldsymbol{x}}_1} & \cdots & \phi_N(\boldsymbol{x})\big|_{\boldsymbol{x}=\bar{\boldsymbol{x}}_1} \\ \vdots & \ddots & \vdots \\ \phi_1(\boldsymbol{x})\big|_{\boldsymbol{x}=\bar{\boldsymbol{x}}_N} & \cdots & \phi_N(\boldsymbol{x})\big|_{\boldsymbol{x}=\bar{\boldsymbol{x}}_N}\end{bmatrix}_{N\times N}\\
\mathbf{Z}_k(\bar{\boldsymbol{x}}, t_k) &= \underset{m,j}{\text{matrix}}\left\{\phi_j(\boldsymbol{x})\Big|_{\boldsymbol{x}=\boldsymbol{f}_{ds}(\bar{\boldsymbol{x}}_m,t_k)+\boldsymbol{g}_{ds}(\bar{\boldsymbol{x}}_m,t_k)\boldsymbol{u}_{ds,k,m}^*}\right\}\\
&= \begin{bmatrix} \phi_1(\boldsymbol{x})\big|_{\boldsymbol{x}=\boldsymbol{f}_{ds}(\bar{\boldsymbol{x}}_1,t_k)+\boldsymbol{g}_{ds}(\bar{\boldsymbol{x}}_1,t_k)\boldsymbol{u}_{ds,k,1}^*} & \cdots & \phi_N(\boldsymbol{x})\big|_{\boldsymbol{x}=\boldsymbol{f}_{ds}(\bar{\boldsymbol{x}}_1,t_k)+\boldsymbol{g}_{ds}(\bar{\boldsymbol{x}}_1,t_k)\boldsymbol{u}_{ds,k,1}^*} \\ \vdots & \ddots & \vdots \\ \phi_1(\boldsymbol{x})\big|_{\boldsymbol{x}=\boldsymbol{f}_{ds}(\bar{\boldsymbol{x}}_N,t_k)+\boldsymbol{g}_{ds}(\bar{\boldsymbol{x}}_N,t_k)\boldsymbol{u}_{ds,k,N}^*} & \cdots & \phi_N(\boldsymbol{x})\big|_{\boldsymbol{x}=\boldsymbol{f}_{ds}(\bar{\boldsymbol{x}}_N,t_k)+\boldsymbol{g}_{ds}(\bar{\boldsymbol{x}}_N,t_k)\boldsymbol{u}_{ds,k,N}^*}\end{bmatrix}_{N\times N}
\end{aligned} \tag{26}$$

2.3 Hybrid Nonlinear Optimal Control Law

Armed with the continuous-time and discrete-time optimal control gain equations, (16) and (25), respectively, the desired hybrid nonlinear optimal control gains can be now computed over the entire operating time through solving the following sets of equations (termed *the hybrid optimal control gain equations*) for $\boldsymbol{C}_N^*(t)$ in an interacting manner:

$$\begin{aligned}
&\dot{\boldsymbol{C}}_N^*(t) + \mathcal{Q}(c^*(t), t)\boldsymbol{C}_N^*(t) + \boldsymbol{d} = \boldsymbol{0}, \quad \boldsymbol{C}_N^*(t_{\mathrm{f}}) = \boldsymbol{0} \quad [\text{See Eq. (17)}] \quad t \neq t_k\\
&\boldsymbol{C}_N^*(t_k^-) = \left(\boldsymbol{\Psi}_k(\bar{\boldsymbol{x}})\right)^{-1}\left[\boldsymbol{W}_k(\bar{\boldsymbol{x}}, t_k) + \mathbf{Z}_k(\bar{\boldsymbol{x}}, t_k)\boldsymbol{C}_N^*(t_k^+)\right] \quad [\text{See Eq. (26)}] \quad t = t_k
\end{aligned} \tag{27}$$

Beginning with the boundary conditions at the terminal time $\boldsymbol{C}_N^*(t_\mathrm{f})$, the continuous-time optimal control gain equations are first integrated backward in time to compute $\boldsymbol{C}_N^*(t)$ between impulsive instants. Once a specific criterion is met, an impulse in then induced in the solution at $t = t_k$ via exciting the discrete-time optimal control gain equations fed by $\boldsymbol{C}_N^*(t_k^+)$ and, in consequence, the continuous evolution of $\boldsymbol{C}_N^*(t)$ is instantaneously switched to discontinuous changes occurring in the discrete-time subsystem. $\boldsymbol{C}_N^*(t_k^-)$ computed at $t = t_k$ is subsequently used as a new set of terminal conditions for the continuous-time set of equations to be integrated backward from t_k^- to t_{k-1}^+. Exhibiting continuous evolution and instantaneous changes on appropriate subsystems, the control gain vector maintains this interacting sequence until the initial time t_0 is reached.

With the hybrid nonlinear optimal control gain vector thus computed, the desired hybrid nonlinear optimal control law can be ultimately formulated as follows:

$$\begin{aligned}
\boldsymbol{u}_{ct}^*(\boldsymbol{x}\,,\,t) &= -\frac{1}{2}\boldsymbol{R}_{ct}^{-1}\boldsymbol{g}_{ct}^{\mathrm{T}}(\boldsymbol{x}\,,\,t)\mathbf{J}_{\boldsymbol{x}}^{\mathrm{T}}\big(\boldsymbol{\Phi}_N(\boldsymbol{x})\big)\boldsymbol{C}_N^*(t) \quad t \neq t_k \\
\boldsymbol{u}_{ds,k}^*(\boldsymbol{x}_k^+,\,t_k^+) &= -\frac{1}{2}\boldsymbol{R}_{ds}^{-1}\boldsymbol{g}_{ds}^{\mathrm{T}}\mathbf{J}_{\boldsymbol{x}}^{\mathrm{T}}\big(\boldsymbol{\Phi}_N(\boldsymbol{x})\big)\Big|_{\boldsymbol{x}=\boldsymbol{x}_k^+}\boldsymbol{C}_N^*(t_k^+) \quad t = t_k
\end{aligned} \tag{28}$$

Presented in Table 1, the proposed hybrid optimal control architecture is summarized and compared to the hybrid LQR control scheme as discussed in [19–21].

Table 1 Hybrid nonlinear optimal control (left column) in comparison with hybrid LQR control (right column)

Hybrid nonlinear optimal control	Hybrid Riccati-based optimal (LQR) control
$\dot{\boldsymbol{x}}(t) = \boldsymbol{f}_{ct}(\boldsymbol{x},t) + \boldsymbol{g}_{ct}(\boldsymbol{x},t)\boldsymbol{u}_{ct}(t),\ \boldsymbol{x}(t_0) = \boldsymbol{x}_0, \quad t \neq t_k$ $\boldsymbol{x}_k^+ = \boldsymbol{f}_{ds}(\boldsymbol{x}_k^-,t) + \boldsymbol{g}_{ds}(\boldsymbol{x}_k^-,t)\boldsymbol{u}_{ds}(t) \quad t = t_k$	$\dot{\boldsymbol{x}}(t) = \boldsymbol{A}_{ct}(t)\boldsymbol{x} + \boldsymbol{B}_{ct}(t)\boldsymbol{u}_{ct}(t),\ \boldsymbol{x}(t_0) = \boldsymbol{x}_0 \quad t \neq t_k$ $\boldsymbol{x}_k^+ = \boldsymbol{A}_{ds}(t)\boldsymbol{x}_k^- + \boldsymbol{B}_{ds}(t)\boldsymbol{u}_{ds}(t) \quad t = t_k$
$\mathcal{J} = \int_{t_0}^{t_\mathrm{f}} \Big(l_{ct}(\boldsymbol{x}) + \|\boldsymbol{u}_{ct}(t)\|_{\boldsymbol{R}_{ct}}^2\Big)\,\mathrm{d}t$ $+ \sum_{k=1}^{\mathcal{K}} \Big(l_{ds}(\boldsymbol{x}_k^-) + \|\boldsymbol{u}_{ds}(t_k)\|_{\boldsymbol{R}_{ds}}^2\Big)$	$\mathcal{J} = \int_{t_0}^{t_\mathrm{f}} \big(\boldsymbol{x}^{\mathrm{T}}\boldsymbol{Q}_{ct}\boldsymbol{x} + \boldsymbol{u}_{ct}^{\mathrm{T}}(t)\boldsymbol{R}_{ct}\boldsymbol{u}_{ct}(t)\big)\,\mathrm{d}t$ $+ \sum_{k=1}^{\mathcal{K}} \Big(\boldsymbol{x}_k^{-\mathrm{T}}\boldsymbol{Q}_{ds}\boldsymbol{x}_k^- + \boldsymbol{u}_{ds}^{\mathrm{T}}(t_k)\boldsymbol{R}_{ds}\boldsymbol{u}_{ds}(t_k)\Big)$
$V_N(\boldsymbol{x}\,,\,t) = \sum_{j=1}^N c_j^*(t)\phi_j(\boldsymbol{x}) = \boldsymbol{\Phi}_N^{\mathrm{T}}(\boldsymbol{x})\boldsymbol{C}_N^*(t)$ $\dot{\boldsymbol{C}}_N^*(t) + \mathcal{Q}(c^*(t),t)\boldsymbol{C}_N^*(t) + \boldsymbol{d} = \boldsymbol{0} \quad , \quad \boldsymbol{C}_N^*(t_\mathrm{f}) = \boldsymbol{0}$ [See Eq. (17)] $\quad t \neq t_k$	$V(\boldsymbol{x}\,,\,t) := \boldsymbol{x}^{\mathrm{T}}\boldsymbol{P}(t)\boldsymbol{x}$ $\dot{\boldsymbol{P}}(t) + \boldsymbol{A}_{ct}^{\mathrm{T}}\boldsymbol{P}(t) + \boldsymbol{P}(t)\boldsymbol{A}_{ct} + \boldsymbol{Q}_{ct}$ $- \boldsymbol{P}(t)\boldsymbol{B}_{ct}\boldsymbol{R}_{ct}^{-1}\boldsymbol{B}_{ct}^{\mathrm{T}}\boldsymbol{P}(t) = \boldsymbol{0},\ \boldsymbol{P}(t_\mathrm{f}) = \boldsymbol{0} \quad t \neq t_k$
$\boldsymbol{C}_N^*(t_k^-) = \big(\boldsymbol{\Psi}_k(\bar{\boldsymbol{x}})\big)^{-1}\big[\boldsymbol{W}_k(\bar{\boldsymbol{x}},t_k) + \mathbf{Z}_k(\bar{\boldsymbol{x}},t_k)\boldsymbol{C}_N^*(t_k^+)\big]$ [See Eq. (26)] $\quad t = t_k$	$\boldsymbol{P}_k^- = -\boldsymbol{A}_{ds}^{\mathrm{T}}\boldsymbol{P}_k^+\boldsymbol{B}_{ds}\big[\boldsymbol{R}_{ds} + \boldsymbol{B}_{ds}^{\mathrm{T}}\boldsymbol{P}_k^+\boldsymbol{B}_{ds}\big]^{-1}\boldsymbol{B}_{ds}^{\mathrm{T}}\boldsymbol{P}_k^+\boldsymbol{A}_{ds}$ $+ \boldsymbol{Q}_{ds} + \boldsymbol{A}_{ds}^{\mathrm{T}}\boldsymbol{P}_k^+\boldsymbol{A}_{ds} \quad t = t_k$
$\boldsymbol{C}_N^*(t)$: Nonlinear optimal gain vector	$\boldsymbol{P}(t)$: Linear optimal gain matrix
$\boldsymbol{u}_{ct}^* = -\frac{1}{2}\boldsymbol{R}_{ct}^{-1}\boldsymbol{g}_{ct}^{\mathrm{T}}(\boldsymbol{x}\,,\,t)\mathbf{J}_{\boldsymbol{x}}^{\mathrm{T}}\big(\boldsymbol{\Phi}_N(\boldsymbol{x})\big)\boldsymbol{C}_N^*(t) \quad t \neq t_k$	$\boldsymbol{u}_{ct}^* = -\boldsymbol{R}_{ct}^{-1}\boldsymbol{B}_{ct}^{\mathrm{T}}(t)\boldsymbol{P}(t)\boldsymbol{x} \quad t \neq t_k$
$\boldsymbol{u}_{ds,k}^* = -\frac{1}{2}\boldsymbol{R}_{ds}^{-1}\boldsymbol{g}_{ds}^{\mathrm{T}}\mathbf{J}_{\boldsymbol{x}}^{\mathrm{T}}\big(\boldsymbol{\Phi}_N(\boldsymbol{x})\big)\Big|_{\boldsymbol{x}=\boldsymbol{x}_k^+}\boldsymbol{C}_N^*(t_k^+) \quad t = t_k$	$\boldsymbol{u}_{ds,k}^* = -\boldsymbol{R}_{ds}^{-1}\boldsymbol{B}_{ds}^{\mathrm{T}}\boldsymbol{A}_{ds}^{-\mathrm{T}}\big[\boldsymbol{P}_k^- - \boldsymbol{Q}_{ds}\big]\boldsymbol{x}_k^- \quad t = t_k$

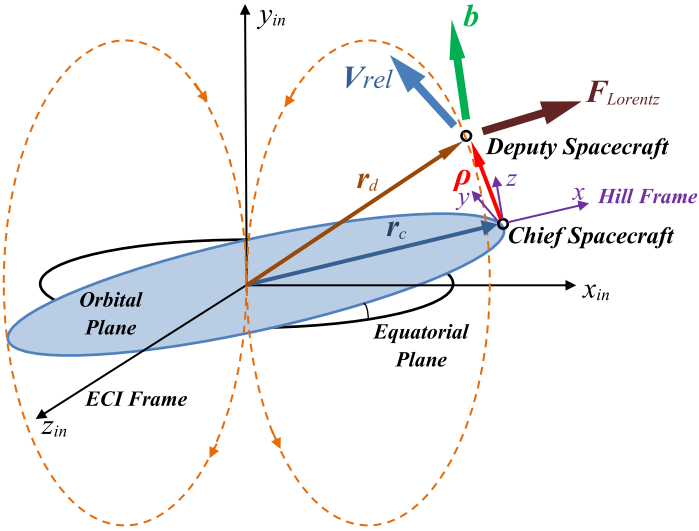

Fig. 1 Schematic representation of Lorentz-augmented spacecraft formation flying in low inclined LEO

3 Spacecraft Formation Flight

As a hybrid dynamical system, the formation flight control system being developed in this paper consists of two interacting modes of operation: the Lorentz force, as the main continuous-time renewable source of actuation, and impulsive thrusting, as an auxiliary discrete-time actuation mechanism. Figure 1 shows a schematic representation of the proposed Lorentz-augmented formation flight in a low inclined LEO involving two satellites referred to as *the chief spacecraft* and *the deputy spacecraft*. The chief satellite orbits the Earth in a reference orbit, either circular or elliptic, whereas the deputy (Lorentz) one orbits the chief spacecraft and is equipped with three thrusters capable of producing force per unit mass along each local frame axis. Furthermore, the Earth-Centered-Inertial (ECI) frame is placed at the center of the Earth, and a local-vertical-local-horizontal frame known as *the Hill frame* is located at the center of mass of the chief spacecraft with x-axis pointing away from the Earth's center and z-axis normal to the orbital plane of the chief spacecraft. Therefore, the electrostatically charged deputy spacecraft are externally propelled in a continuous manner by the Lorentz force arising primarily from the interaction with the Earth magnetic field. Nevertheless, once a certain criterion is met, the Lorentz actuation is instantaneously switched to impulsive thrusting and, in consequence, a triple set of impulsive force, one along each direction of the Hill frame, is then applied to each deputy spacecraft by expulsion devices (thrusters). The motion of the deputy spacecraft relative to the chief satellite is therefore characterized by a continuous-time set of differential equations, which characterizes the relative orbital motion of the

dynamical system between impulsive events, and a discrete-time set of difference equations, which governs instantaneous changes in the system state once an impulse occurs.

Assuming the deputy spacecraft are only actuated in the formation flight in question, as noted above, the differential equations governing the *exact* orbital motion of the chief and deputy spacecraft in the ECI coordinate system are thus described by Newton's law of gravitation [7]:

$$\ddot{\boldsymbol{r}}_{c,in} = -\frac{\mu_{\oplus}}{r_c^3}\boldsymbol{r}_{c,in} + \boldsymbol{f}_{pb,in}(\boldsymbol{r}_{c,in}) \tag{29}$$

$$\ddot{\boldsymbol{r}}_{d,in} = -\frac{\mu_{\oplus}}{r_d^3}\boldsymbol{r}_{d,in} + \boldsymbol{f}_{pb,in}(\boldsymbol{r}_{d,in}) + \boldsymbol{f}_{Ltz,in} + \boldsymbol{f}_{imp,in} \tag{30}$$

where $\mu_{\oplus} = 3.98593 \times 10^{14}\,\mathrm{m}^3/\mathrm{s}^2$ is the Earth standard gravitational parameter, $\boldsymbol{r}_{c,in}$ and $\boldsymbol{r}_{d,in}$ represent, respectively, the *exact* inertial positions of the chief and deputy spacecraft from the center of the Earth, and r_c and r_d specify their scalar radii. Furthermore, $\boldsymbol{f}_{Ltz,in}$ and $\boldsymbol{f}_{imp,in}$ define, respectively, the continuous-time (Lorentz) and discrete-time control force per unit mass expressed in the ECI reference frame which can be obtained by:

$$\boldsymbol{f}_{Ltz,in} = \frac{q}{m_d}\left(\boldsymbol{E}_{in} + \boldsymbol{v}_{rel,in}^{\times}\boldsymbol{b}_{in}\right) \tag{31}$$

$$\boldsymbol{f}_{imp,in} = \sum_{k=1}^{\mathcal{K}} \boldsymbol{n}_{in}\delta(t - t_k) \tag{32}$$

where $\hat{q} = q/m_d$, defined as the charge per unit mass of the deputy spacecraft (also referred to as *the specific charge*), is the continuous-time control input, $\boldsymbol{E}_{in}$ denotes the electrical field strength, $\boldsymbol{v}_{rel,in}$ refers to the relative velocity of the deputy spacecraft with respect to the Earth magnetic field, $\boldsymbol{b}_{in}$ indicates the Earth magnetic field, and $(\cdot)^{\times}$ represents the skew-symmetric matrix used to implement the cross-product. Moreover, the Dirac delta function, $\delta(t)$, located at each impulsive instant, $t = t_k$, is employed in conjunction with the discrete-time gain values, $\boldsymbol{n}_{in}$, to represent the discrete-time force per unit mass. In addition, the perturbation force per unit mass with spatial dependence denoted by $\boldsymbol{f}_{pb,in}$ in (29) and (30) can be calculated by [7]:

$$\boldsymbol{f}_{pb,in} = \frac{3\mu_{\oplus}J_2R_{\oplus}^2}{2r^5}\left[\left(5\frac{\left(\boldsymbol{r}_{in}^{\mathrm{T}}\hat{\boldsymbol{z}}_{in}\right)^2}{r^2} - 1\right)\boldsymbol{r}_{in} - 2\left(\boldsymbol{r}_{in}^{\mathrm{T}}\hat{\boldsymbol{z}}_{in}\right)\hat{\boldsymbol{z}}_{in}\right] \tag{33}$$

where $J_2 = 1.083 \times 10^{-3}$ represents the J_2-effect perturbations due to the Earth oblateness, $R_{\oplus}$ is the Earth radius, and $\hat{\boldsymbol{z}}_i = \begin{bmatrix} 0 & 0 & 1 \end{bmatrix}^{\mathrm{T}}$ denotes the basis vector along the z-axis of the ECI frame. Assuming $\boldsymbol{E}_{in}$ is negligible, (31) can be rewritten by expanding $\boldsymbol{v}_{rel,in}$ in terms of the position and velocity vectors of the deputy spacecraft as follows:

$$\boldsymbol{f}_{Ltz,in} \cong \hat{q}\left(\boldsymbol{v}_{d,in} - \boldsymbol{\omega}^{\times}_{\oplus,in}\boldsymbol{r}_{d,in}\right)^{\times}\boldsymbol{b}_{in} \tag{34}$$

where $\boldsymbol{\omega}_{\oplus,in} = 360.9856\hat{\boldsymbol{z}}_i$ deg/day are the inertial components of the Earth angular velocity about its own axis of rotation. Furthermore, $\boldsymbol{r}_{d,in}$ and $\boldsymbol{v}_{d,in}$, respectively, denote the inertial position and velocity vectors of the deputy spacecraft which can be defined as follows:

$$\boldsymbol{r}_{d,in} = \boldsymbol{r}_{c,in} + \boldsymbol{\rho}_{in} = \boldsymbol{r}_{c,in} + \mathcal{R}_{in-hl}\boldsymbol{\rho}_{hl} \tag{35}$$

$$\boldsymbol{v}_{d,in} = \boldsymbol{v}_{c,in} + \dot{\boldsymbol{\rho}}_{in} = \boldsymbol{v}_{c,in} + \dot{\mathcal{R}}_{in-hl}\boldsymbol{\rho}_{hl} + \mathcal{R}_{in-hl}\dot{\boldsymbol{\rho}}_{hl} \tag{36}$$

where $\boldsymbol{\rho}_{in}$ represents the relative coordinates of the deputy spacecraft with respect to the chief satellite in the ECI frame, and $\boldsymbol{\rho}_{hl} = \begin{bmatrix} x & y & z \end{bmatrix}^{\mathrm{T}}$ specifies the relative position of the deputy spacecraft in the Hill frame. Since the orbital motion of the deputy spacecraft relative to the chief satellite is described in the Hill frame, the foregoing quantities expressed in the inertial coordinate system must be transferred to the Hill frame. To this end, two separate time-dependent and state-dependent rotation matrices, along with their time derivatives, from the ECI frame to the Hill frame can be employed, depending upon the character of the orbital motion in question. The first rotation matrix, the application of which is essentially restricted to the Keplerian orbits, can be obtained through three successive rotations as follows [7]:

$$\mathcal{R}_{in-hl}(t) = \mathcal{R}_z(\hat{u})\mathcal{R}_x(\hat{i})\mathcal{R}_z(\hat{\Omega}) \tag{37}$$

$$\dot{\mathcal{R}}_{in-hl}(t) = -\boldsymbol{\omega}^{\times}_{hi}\mathcal{R}_{in-hl}(t) \tag{38}$$

where $\hat{u}$, $\hat{i}$, and $\hat{\Omega}$ represent, respectively, the argument of latitude, inclination, and the right ascension of the ascending node for the chief spacecraft. Furthermore, $\mathcal{R}_x(\cdot)$ and $\mathcal{R}_z(\cdot)$ denote the principal rotation matrices about the x and z axes, respectively, and $\boldsymbol{\omega}_{hl-in} = \begin{bmatrix} 0 & 0 & \dot{\hat{u}} \end{bmatrix}^{\mathrm{T}}$.

In contrast to the first set, the second rotation matrix, which accounts for the J_2-effect perturbations, can be used for both Keplerian and non-Keplerian orbits [27]:

$$\mathcal{R}_{in-hl}(\boldsymbol{r}_{c,in}, \boldsymbol{v}_{c,in}) = \begin{bmatrix} \dfrac{\boldsymbol{r}_{c,in}}{\|\boldsymbol{r}_{c,in}\|} & \dfrac{\boldsymbol{h}^{\times}_{c,in}\boldsymbol{r}_{c,in}}{\|\boldsymbol{h}^{\times}_{c,in}\boldsymbol{r}_{c,in}\|} & \dfrac{\boldsymbol{h}_{c,in}}{\|\boldsymbol{h}_{c,in}\|} \end{bmatrix}^{\mathrm{T}} \tag{39}$$

$$\dot{\mathcal{R}}_{in-hl} = \begin{bmatrix} \dfrac{\boldsymbol{v}_{c,in}}{\|\boldsymbol{r}_{c,in}\|} - \dfrac{\boldsymbol{r}^{\mathrm{T}}_{c,in}\boldsymbol{v}_{c,in}\boldsymbol{r}_{c,in}}{\|\boldsymbol{r}_{c,in}\|^3} & \dfrac{\dot{(\boldsymbol{h}^{\times}_{c,in}\boldsymbol{r}_{c,in})}}{\|\boldsymbol{h}^{\times}_{c,in}\boldsymbol{r}_{c,in}\|} - \dfrac{(\boldsymbol{h}^{\times}_{c,in}\boldsymbol{r}_{c,in})^{\mathrm{T}}\dot{(\boldsymbol{h}^{\times}_{c,in}\boldsymbol{r}_{c,in})}(\boldsymbol{h}^{\times}_{c,in}\boldsymbol{r}_{c,in})}{\|\boldsymbol{h}^{\times}_{c,in}\boldsymbol{r}_{c,in}\|^3} & \dfrac{\boldsymbol{h}_{c,in}}{\|\boldsymbol{h}_{c,in}\|} - \dfrac{\boldsymbol{h}^{\mathrm{T}}_{c,in}\boldsymbol{h}_{c,in}\boldsymbol{h}_{c,in}}{\|\boldsymbol{h}_{c,in}\|^3} \end{bmatrix}^{\mathrm{T}} \tag{40}$$

where $\boldsymbol{h}_{c,in} = \boldsymbol{r}^{\times}_{c,in}\boldsymbol{v}_{c,in}$ denotes the inertial orbital angular momentum of the chief spacecraft as one of the fundamental constants of the orbital motion which specifies the orbital plane. In this paper, the abovementioned rotation matrices are employed,

respectively, for control design (where the reference orbit is assumed to be Keplerian) and numerical simulations (which consider the J_2-effect perturbations). Furthermore, a non-tilted dipole model of the geomagnetic field as described in [29] is also used in this paper to estimate the inertial magnetic field vector, $\boldsymbol{b}_{in}$.

The relative dynamics characterizing the orbital motion of the deputy spacecraft with respect to the chief satellite in the ECI frame can be now developed in terms of $\boldsymbol{r}_{c,in}$ and $\boldsymbol{\rho}_{in}$ by subtracting (29) from (30) as follows:

$$\begin{aligned}\ddot{\boldsymbol{\rho}}_{in} &= \ddot{\boldsymbol{r}}_{d,in} - \ddot{\boldsymbol{r}}_{c,in} \\ &= -\frac{\mu_{\oplus}}{\|\boldsymbol{r}_{c,in} + \boldsymbol{\rho}_{in}\|^3}(\boldsymbol{r}_{c,in} + \boldsymbol{\rho}_{in}) + \frac{\mu_{\oplus}}{r_c^3}\boldsymbol{r}_{c,in} + \boldsymbol{f}_{pb,in}(\boldsymbol{r}_{c,in} + \boldsymbol{\rho}_{in}) - \boldsymbol{f}_{pb,in}(\boldsymbol{r}_{c,in}) + \boldsymbol{f}_{Ltz,in} + \boldsymbol{f}_{imp,in}\end{aligned} \tag{41}$$

Omitting the details, the equations of relative motion in the Hill frame accommodating the nonlinearity of the differential gravitational accelerations under the assumption of a circular Keplerian reference orbit can be thus formulated by [28]:

$$\begin{aligned}&\ddot{x} - 2n_o\dot{y} - 3n_o^2 x - (3\mu_{\oplus}/2a_c^4)(y^2 + z^2 - 2x^2) = f_{Ltz,x,hl} + f_{imp,x,hl} \\ &\ddot{y} + 2n_o\dot{x} - (3\mu_{\oplus}/a_c^4)xy = f_{Ltz,y,hl} + f_{imp,y,hl} \\ &\ddot{z} + n_o^2 z - (3\mu_{\oplus}/a_c^4)xz = f_{Ltz,z,hl} + f_{imp,z,hl}\end{aligned} \tag{42}$$

where $\boldsymbol{x} = \left[\boldsymbol{\rho}_{hl}^{\mathrm{T}}\ \dot{\boldsymbol{\rho}}_{hl}^{\mathrm{T}}\right]^{\mathrm{T}} = \left[x\ y\ z\ \dot{x}\ \dot{y}\ \dot{z}\right]^{\mathrm{T}}$, n_o denotes the orbital mean motion, and a_c refers to the semi-major axis for the orbital motion of the chief spacecraft.

Assuming that the chief spacecraft travels in a circular Keplerian reference orbit at an altitude of 714 km, the classical orbital elements describing the resultant orbital motion are defined as:

$$\left\{a_c\,,\ e\,,\ \hat{i},\ \hat{\Omega}\,,\ \hat{\omega}\,,\ t_0\right\} = \{7092\,\mathrm{km}\,,\ 0\,,\ 3^\circ,\ 0,\ 0,\ 0\}$$

where e, $\hat{\omega}$, and t_0 refer, respectively, to eccentricity, the argument of perigee, and the time of perigee passage.

4 Practical Considerations

With the relative motion dynamics expressed in the Hill frame thus derived, the hybrid nonlinear optimal control framework developed in Sect. 2 can be now exploited to accomplish the main objective; that is, to maintain bounded relative motion between the deputy and chief spacecraft in formation. However, the proposed control scheme is structurally restricted to serve as a regulator and, in consequence, all the components of the state and control must converge to zero as time approaches to t_{f}. In order to employ the control architecture in question for tracking control synthesis, a change of variables must take place for both state and control vectors. With this objective in view, error variables of the form $\tilde{\boldsymbol{x}} = \boldsymbol{x} - \boldsymbol{x}_{des}$ and $\tilde{\boldsymbol{u}} = \boldsymbol{u} - \boldsymbol{u}_{ss}$ corresponding to state and control vectors, where $\boldsymbol{x}_{des} = \left[x_{des}\ y_{des}\ z_{des}\ \dot{x}_{des}\ \dot{y}_{des}\ \dot{z}_{des}\right]^{\mathrm{T}}$ denotes the desired trajectory and $\boldsymbol{u}_{ss}$

represents the control input in the steady-state phase, are first defined, and the relative dynamics represented by (42) are then rewritten in terms of relative errors. Defining $\tilde{\boldsymbol{x}} = \left[\mathrm{x}_1\ \mathrm{x}_2\ \mathrm{x}_3\ \mathrm{x}_4\ \mathrm{x}_5\ \mathrm{x}_6\right]^{\mathrm{T}} = \left[\tilde{x}\ \tilde{y}\ \tilde{z}\ \dot{\tilde{x}}\ \dot{\tilde{y}}\ \dot{\tilde{z}}\right]^{\mathrm{T}}$, the resultant nonlinear dynamics characterizing the relative motion of the deputy spacecraft with respect to the chief satellite in the Hill frame can be thus formulated in a state-space representation with continuous-time and discrete-time system functions of the following form:

$$\boldsymbol{f}_{ct}(\tilde{\boldsymbol{x}},t) = \begin{bmatrix} \mathrm{x}_4 \\ \mathrm{x}_5 \\ \mathrm{x}_6 \\ 3n_o^2(\mathrm{x}_1 + x_{des}) + (3\mu_{\oplus}/2a_c^4)\left(-2(\mathrm{x}_1 + x_{des})^2 + (\mathrm{x}_2 + y_{des})^2 + (\mathrm{x}_3 + z_{des})^2\right) + 2n_o(\mathrm{x}_5 + \dot{y}_{des}) - \ddot{x}_{des} \\ (3\mu_{\oplus}/a_c^4)(\mathrm{x}_1 + x_{des})(\mathrm{x}_2 + y_{des}) - 2n_o(\mathrm{x}_4 + \dot{x}_{des}) - \ddot{y}_{des} \\ (3\mu_{\oplus}/a_c^4)(\mathrm{x}_1 + x_{des})(\mathrm{x}_3 + z_{des}) - n_o^2(\mathrm{x}_3 + z_{des}) - \ddot{z}_{des} \end{bmatrix} + \begin{bmatrix} \boldsymbol{0}_{3\times 1} \\ \mathcal{R}_{in-hl}(\boldsymbol{r}_{c,in}, \boldsymbol{v}_{c,in})\left(\boldsymbol{v}_{d,in}|_{\boldsymbol{x}=\boldsymbol{x}_{des}} - \boldsymbol{\omega}_{\oplus,in}^{\times}\boldsymbol{r}_{d,in}|_{\boldsymbol{x}=\boldsymbol{x}_{des}}\right)^{\times}\boldsymbol{b}_{in}(\boldsymbol{r}_{c,in}) \end{bmatrix} u_{ct,ss} \tag{43}$$

$$\boldsymbol{g}_{ct}(\tilde{\boldsymbol{x}},t) = \begin{bmatrix} \boldsymbol{0}_{3\times 1} \\ \mathcal{R}_{in-hl}(\boldsymbol{r}_{c,in}, \boldsymbol{v}_{c,in})\left(\boldsymbol{v}_{d,in} - \boldsymbol{\omega}_{\oplus,in}^{\times}\boldsymbol{r}_{d,in}\right)^{\times}\boldsymbol{b}_{in}(\boldsymbol{r}_{c,in}) \end{bmatrix} \tag{44}$$

$$\boldsymbol{f}_{ds}(\tilde{\boldsymbol{x}}_k^-, t_k) = \boldsymbol{f}_{ds}(\tilde{\boldsymbol{x}}_k^-) = \tilde{\boldsymbol{x}}_k^- \tag{45}$$

$$\boldsymbol{g}_{ds}(\tilde{\boldsymbol{x}}_k^-, t_k) = \boldsymbol{g}_{ds} = \begin{bmatrix} \boldsymbol{0}_{3\times 3} \\ \boldsymbol{1}_{3\times 3} \end{bmatrix} \tag{46}$$

where $u_{ct,ss}$ and $\boldsymbol{u}_{ds,k,ss}$, which correspond to the continuous-time and discrete-time control inputs in the steady-state phase, respectively, can be computed according to (42) as follows:

$$u_{ct,ss} = (\boldsymbol{g}_{ss}^{\mathrm{T}}\boldsymbol{g}_{ss})^{-1}\boldsymbol{g}_{ss}^{\mathrm{T}}\boldsymbol{f}_{ss} \tag{47}$$

$$\boldsymbol{u}_{ds,k,ss} = (\boldsymbol{g}_{ds}^{\mathrm{T}}\boldsymbol{g}_{ds})^{-1}\boldsymbol{g}_{ds}^{\mathrm{T}}\left(\boldsymbol{x}_{des}(t_k^+) - \boldsymbol{x}_{des}(t_k^-)\right) \tag{48}$$

with

$$\boldsymbol{f}_{ss}(t) = \begin{bmatrix} \ddot{x}_{des} - 2n_o\dot{y}_{des} - 3n_o^2 x_{des} - (3\mu_{\oplus}/2a_c^4)(y_{des}^2 + z_{des}^2 - 2x_{des}^2) \\ \ddot{y}_{des} + 2n_o\dot{x}_{des} - (3\mu_{\oplus}/a_c^4)x_{des}y_{des} \\ \ddot{z}_{des} + n_o^2 z_{des} - (3\mu_{\oplus}/a_c^4)x_{des}z_{des} \end{bmatrix} \tag{49}$$

$$\boldsymbol{g}_{ss}(t) = \mathcal{R}_{in-hl}(\boldsymbol{r}_{c,in}, \boldsymbol{v}_{c,in})\left(\boldsymbol{v}_{d,in}\big|_{\boldsymbol{x}=\boldsymbol{x}_{des}} - \boldsymbol{\omega}^{\times}_{\oplus,in}\boldsymbol{r}_{d,in}\big|_{\boldsymbol{x}=\boldsymbol{x}_{des}} \right)^{\times} \boldsymbol{b}_{in}(\boldsymbol{r}_{c,in}) \tag{50}$$

As with any tracking control synthesis, the main control objective here is to maintain bounded relative motion between spacecraft in formation by tracking a desired trajectory while simultaneously rejecting external perturbations. One particular formation of interest, as a desired trajectory candidate, can be defined by the exact solution to the Hill-Clohessy-Wiltshire (HCW) equations of the following form [6]:

$$\begin{cases} \ddot{x} - 2n_o\dot{y} - 3n_o^2 x = 0 \\ \ddot{y} + 2n_o\dot{x} = 0 \\ \ddot{z} + n_o^2 z = 0 \end{cases} \tag{51}$$

The HCW equations, in fact, model the uncontrolled relative motion dynamics under the three fundamental assumptions: the linearized differential gravitational accelerations, a circular reference orbit, and the spherical Earth (without J_2-effect perturbations) [28]. As an interesting character of the trajectory resulted from the HCW equations, the derived relative orbit reduces to a circular orbit when projected on the y–z plane of the Hill frame, hence termed *the projected circular relative orbits* (PCRO) [6, 28]. The PCRO solutions represented in the following are therefore selected in this paper as a desired trajectory to be followed by the deputy spacecraft to attain mission objectives:

$$\boldsymbol{x}_{PCRO}(t) = \left[x_{PCRO} \;\; y_{PCRO} \;\; z_{PCRO} \;\; \dot{x}_{PCRO} \;\; \dot{y}_{PCRO} \;\; \dot{z}_{PCRO} \right]^{\mathrm{T}} \tag{52}$$

with

$$x_{PCRO}(t) = (R_{PCRO}/2)\sin(n_o t + \alpha_0) \tag{53}$$

$$y_{PCRO}(t) = R_{PCRO}\cos(n_o t + \alpha_0)$$

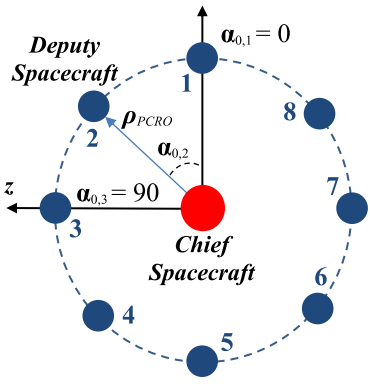

Fig. 2 Snapshot of formation flight involving 8 deputy spacecraft with $\alpha_{0,1}$ at the perigee of the chief spacecraft [28]

$$z_{PCRO}(t) = R_{PCRO} \sin(n_o t + \alpha_0)$$

where R_{PCRO} determines the size of the relative orbit and α_0 denotes an initial phase angle. In this regard, each deputy spacecraft in formation is assigned a unique α_0. Figure 2 depicts a schematic representation of 8 deputy spacecraft in formation with $\alpha_{0,1}$ at the perigee of the chief spacecraft.

With the system functions describing the hybrid nonlinear time-dependent dynamical system in question thus discussed, three important structural parameters, the judicious selection of which is required to accurately approximate the value function in each subsystem, remain to be determined:

- A compact set that contains the origin as an interior point and is preferably symmetric about it,
- A set of basis functions that can adequately approximate the value function, and
- A set of collocation points that are located inside and on the boundaries of the compact set.

The compact set (or stability region or a bounded domain of the state space), $\mathbf{\Omega}$, is defined as the domain of possible values for the state. $\mathbf{\Omega}$ can be determined according to kinematical or practical limitations of the system, together with the likely deviation of the system state from its nominal value of zero. Since both relative error position and velocity vectors are free to deviate from their nominal value of zero, their domain of possible values is accordingly elected on the basis of practical considerations as follows:

$$\begin{aligned}\mathbf{\Omega} = &\left[-5000\ \ 5000\right]_{\mathrm{x}_1} \times \left[-5000\ \ 5000\right]_{\mathrm{x}_2} \times \left[-5000\ \ 5000\right]_{\mathrm{x}_3} \\ &\times \left[-5\ \ 5\right]_{\mathrm{x}_4} \times \left[-5\ \ 5\right]_{\mathrm{x}_5} \times \left[-5\ \ 5\right]_{\mathrm{x}_6}\end{aligned}$$

where x_1 to x_3 and x_4 to x_6 are expressed, respectively, in m and m/s.

Proper selection of the basis functions is critical to design of the nonlinear optimal controllers. Two important requirements pertaining to the structure and number of basis elements, namely *characteristic* and *quantity requirements*, must be satisfied in order to make an appropriate choice of basis functions. The main objective being pursued by the characteristic requirement is to synthesize a controller by which the essential nonlinear terms involved in the system dynamics are spanned by the basis functions, and hence effectively captured. Basis elements are therefore configured such that the constituent linear and nonlinear terms of the system dynamics are incorporated into the optimal control law. The resultant controller therefore wields authority to compensate adequately for the nonlinear dynamics of the system. Furthermore, the number of the basis elements must be sufficiently large to approximate the value function with sufficient accuracy (*quantity requirement*). In addition to the characteristic and quantity requirements stressed in the preceding, appropriate selection of basis functions must also render $\langle \mathbf{\Phi}_N, \mathbf{\Phi}_N \rangle_{\mathbf{\Omega}}$ invertible.

As demonstrated in the literature, polynomials have been proven to serve effectively as basis functions in algorithms where the Galerkin-based projection is used

to approximate steady-state versions of the HJB [3, 4] and Hamilton–Jacobi–Isaac [5] equations. To the knowledge of the authors, the best way to find appropriate selection of basis functions for time-dependent dynamical systems is to commence with the quadratic basis elements obtained by the second-order expansion of the system state, eliminating those terms whose corresponding control gains are either zero or very small as compared to the other terms. The remaining quadratic basis elements must be then augmented by further higher-order terms to capture the essential nonlinear dynamics of the system. Due to multiplication of $\boldsymbol{g}_{ct}^{\mathrm{T}}(\boldsymbol{x}\,,\,t)$ and $\boldsymbol{g}_{ds}^{\mathrm{T}}(\boldsymbol{x}_k\,,\,t_k)$ with $\mathbf{J}_{\boldsymbol{x}}^{\mathrm{T}}\big(\boldsymbol{\Phi}_N(\boldsymbol{x})\big)$ in the configuration of the proposed optimal control laws, these additional higher-order basis elements must be selected such that their partial derivatives with respect to *gain-effective states* (those states which correspond to nonzero elements of $\boldsymbol{g}_{ct}$ and $\boldsymbol{g}_{ds}$, thereby contributing substantially to preserve nonzero control gains) result in functions of the states desired to ultimately appear in the abovementioned control laws in order to capture the dominant nonlinear dynamics of the system. By increasing the number of basis elements in a manner consistent with the characteristic requirement, $V_N(\boldsymbol{x}\,,\,t)$ gradually approaches to $V(\boldsymbol{x}\,,\,t)$. At a certain number of basis elements, the performance index ultimately converges and, in consequence, the quantity requirement is fulfilled, i.e., $V_N \cong V$. Henceforth, any further increase in the number of basis elements yields insignificant improvement in the system performance at the expense of computational cost. This process requires a deep understanding of the dynamical behavior of the system in question, as well as some trial and error.

By considering the structure of $\boldsymbol{g}_{ct}(\tilde{\boldsymbol{x}},t)$ and $\boldsymbol{g}_{ds}(\tilde{\boldsymbol{x}}_k\,,\,t_k)$ for the hybrid formation flight control system being developed, as represented in (44) and (46), x_4, x_5, and x_6 serve as the gain-effective states for this dynamical system. Therefore, any basis element involving either x_4, x_5, and x_6 (or their combinations) will ultimately emerge in the nonlinear optimal control law as demonstrated below for the continuous-time subsystem:

$$
\begin{aligned}
u_{ct}^{*}(\tilde{\boldsymbol{x}}\,,\,t) &= -\frac{1}{2}R_{ct}^{-1}\begin{bmatrix}0 & 0 & 0 & g_4 & g_5 & g_6\end{bmatrix}\begin{bmatrix}\frac{\partial\phi_1}{\partial \mathrm{x}_1} & \cdots & \frac{\partial\phi_N}{\partial \mathrm{x}_1}\\ \vdots & & \vdots\\ \frac{\partial\phi_1}{\partial \mathrm{x}_6} & \cdots & \frac{\partial\phi_N}{\partial \mathrm{x}_6}\end{bmatrix}\begin{bmatrix}c_1^{*}(t)\\ \vdots\\ c_N^{*}(t)\end{bmatrix}\\
&= -\frac{1}{2}R_{ct}^{-1}\begin{bmatrix} g_4\frac{\partial\phi_1}{\partial \mathrm{x}_4}+g_5\frac{\partial\phi_1}{\partial \mathrm{x}_5}+g_6\frac{\partial\phi_1}{\partial \mathrm{x}_6} & \cdots & g_4\frac{\partial\phi_N}{\partial \mathrm{x}_4}+g_5\frac{\partial\phi_N}{\partial \mathrm{x}_5}+g_6\frac{\partial\phi_N}{\partial \mathrm{x}_6}\end{bmatrix}\begin{bmatrix}c_1^{*}(t)\\ \vdots\\ c_N^{*}(t)\end{bmatrix}
\end{aligned}
$$

where g_4, g_5, and g_6 represent nonzero elements of $\boldsymbol{g}_{ct}$. Basis elements must be therefore selected such that their partial derivatives with respect to x_4, x_5, and x_6 give rise to functions of $\tilde{\boldsymbol{x}}$ desired to be incorporated into the optimal control law. Due to the presence of five nonlinear terms in the relative error dynamics, namely x_1^2, x_2^2, x_3^2, $\mathrm{x}_1\mathrm{x}_2$, and $\mathrm{x}_1\mathrm{x}_3$, the quadratic basis elements obtained by the second-order expansion of the relative error states must be therefore augmented by additional higher-order terms to capture the aforementioned nonlinear terms, while simultaneously guaranteeing the accuracy of the approximation. To this end, $\mathrm{x}_1^2\mathrm{x}_2\mathrm{x}_4$, $\mathrm{x}_2^2\mathrm{x}_5^2$, and $\mathrm{x}_1\mathrm{x}_3^2\mathrm{x}_6$, among all possible choices, are appended to the resultant quadratic basis

elements to endow the tracking feedback optimal controller with enhanced capabilities to compensate adequately for the system nonlinearities. In view of the preceding guidelines, the following 24 basis elements are consequently elected for the formation flight control system in question to satisfy both characteristic and quantity requirements:

$$\begin{aligned}\boldsymbol{\Phi}_{\mathrm{N}}(\tilde{\boldsymbol{x}}) = \big\{ & \mathrm{x}_1^2,\ \mathrm{x}_1\mathrm{x}_2,\ \mathrm{x}_1\mathrm{x}_3,\ \mathrm{x}_1\mathrm{x}_4,\ \mathrm{x}_1\mathrm{x}_5,\ \mathrm{x}_1\mathrm{x}_6,\ \mathrm{x}_2^2,\ \mathrm{x}_2\mathrm{x}_3,\ \mathrm{x}_2\mathrm{x}_4,\\ & \mathrm{x}_2\mathrm{x}_5,\ \mathrm{x}_2\mathrm{x}_6,\ \mathrm{x}_3^2,\ \mathrm{x}_3\mathrm{x}_4,\ \mathrm{x}_3\mathrm{x}_5,\ \mathrm{x}_3\mathrm{x}_6,\\ & \mathrm{x}_4^2,\ \mathrm{x}_4\mathrm{x}_5,\ \mathrm{x}_4\mathrm{x}_6,\ \mathrm{x}_5^2,\ \mathrm{x}_5\mathrm{x}_6,\ \mathrm{x}_6^2\ ,\ \mathrm{x}_1^2\mathrm{x}_2\mathrm{x}_4,\ \mathrm{x}_2^2\mathrm{x}_5^2,\ \mathrm{x}_1\mathrm{x}_3^2\mathrm{x}_6\big\}\end{aligned}$$

A suitable set of collocation points $\bar{\boldsymbol{x}} = \underset{m}{\mathrm{row}}\left\{\bar{\boldsymbol{x}}_m\right\}$, where $\bar{\boldsymbol{x}}_m \in \mathbb{R}^6$ and $m = 1, \ldots, 24$, is also necessary to synthesize the discrete-time optimal controller. Collocation points can be selected from the entire compact set excluding the origin, provided that the rank condition required to produce an invertible $\boldsymbol{\Psi}_k(\bar{\boldsymbol{x}})$ in (25) is satisfied.

Furthermore, the following set of firing time instants, the application of which suggests satisfactory performance for the formation flying control system in question, is selected; that is, eight equally spaced impulses per orbit ($\mathcal{K} = 8$) in terms of true anomaly beginning at $\theta_1 = 10°$:

$$\begin{aligned}\left\{\theta_1,\ \ldots\ ,\ \theta_{\mathcal{K}}\right\} &= \left\{\theta_1,\ \theta_1 + (360°/\mathcal{K}),\ \ldots\ ,\ \theta_1 + (\mathcal{K}-1)(360°/\mathcal{K})\right\}_{\theta_1=10°,\ \mathcal{K}=8}\\ &= \{10°,\ 55°,\ 100°,\ 145°,\ 190°,\ 235°,\ 280°,\ 325°\}\end{aligned}$$

where θ_1 denotes the true anomaly at which the first impulse is applied.

In addition to the structural parameters discussed in the preceding, two ingredients are essentially required to implement the proposed hybrid feedback tracking controller: the time-varying control gains and the true relative state vector of the deputy spacecraft with respect to the chief satellite. Whereas the former must be calculated prior to implementation, the latter is estimated onboard. Once $\boldsymbol{C}_N^*(t)$ are determined through solving (27) in an interacting manner, they can be used in

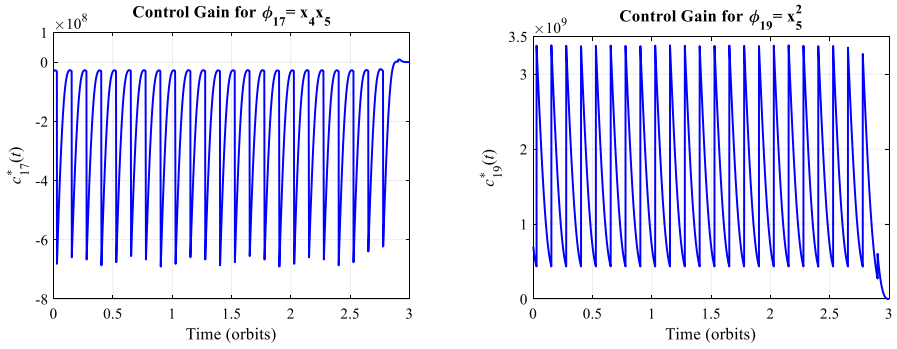

Fig. 3 Periodic evolution of hybrid optimal control gains associated with $\mathrm{x}_4\mathrm{x}_5$ and x_5^2 in accordance with system dynamics

conjunction with the foregoing true relative state vector to construct the feedback tracking controller and run in real time.

Due to intimate connection between state-dependent basis functions, $\{\phi_j(\boldsymbol{x})\}_1^N$, and time-dependent control gains, $\left\{c_j^*(t)\right\}_{j=1}^N$, in forming a discretized representation of $V(\boldsymbol{x}, t)$, each $c_j^*(t)$ evolves in complete harmony with the character of its entangled basis element $\phi_j(\boldsymbol{x})$, while simultaneously duplicating the system dynamics in an intimate manner. As the relative error dynamics involve a periodic function, namely $\boldsymbol{g}_{ct}$ comprised of the Earth magnetic field vector, the time-varying control gains evolve periodically in compliance with the system periodicity. Owing to the very periodic nature of the optimal control gains, Fourier series [17] can be thus employed to approximate the steady-state part of $\boldsymbol{C}_N^*(t)$ by discarding their initial transient phase coming backward from t_f. As a direct consequence, not only is the storage memory requirement significantly reduced via storing the Fourier-based approximate coefficients, instead of the entire time history of $\boldsymbol{C}_N^*(t)$, onboard; but $\boldsymbol{C}_N^*(t)$ are also no longer restricted to the time interval from 0 to t_f (defined by the user for control design). The resultant optimal control gains can be therefore extended globally to any desired operating time of an arbitrary length, hence global asymptotic performance. Figure 3 illustrates the periodic evolution of the optimal control gains corresponding to two randomly selected basis elements, namely $\mathrm{x}_4\mathrm{x}_5$ and x_5^2, over time for the hybrid nonlinear formation flight control system.

5 Numerical Simulations

The tracking performance of the hybrid nonlinear optimal controller developed in Sect. 2 is evaluated in this section via numerical simulations for formation flight involving a relative orbit of the size 10 km configured at the perigee of the chief spacecraft, i.e., $R_{PCRO} = 10$ km and $\alpha_0 = 0$. The main objective here is to synthesize a hybrid pair of feedback tracking control inputs to maintain bounded relative motion between the deputy and chief spacecraft in formation flight in the presence of two factors; the J_2-effect perturbations, which cause formation to drift apart over time, and large initial conditions, which produce a secular growth in the relative motion, hence unbounded departure from the desired trajectory. To this end, the hybrid set of optimal control gain equations given by (27) is first fed by appropriate ingredients and then solved in an interacting manner for $\boldsymbol{C}_N^*(t)$. The resultant optimal control gains are subsequently injected into both continuous-time and discrete-time portions of the hybrid optimal control law represented by (28). Proceeding to the simulation phase, the *exact* differential equations of motion characterizing the non-Keplerian inertial orbital motion of the chief and deputy spacecraft in formation under the influence of the J_2-effect orbital perturbations, i.e., (29) and (30) written in a coupled state-space representation, are then integrated forward simultaneously using a RK4 solver [17].

With the structural parameters $\boldsymbol{\Omega}$, $\boldsymbol{\Phi}_\mathrm{N}(\tilde{\boldsymbol{x}})$, $\bar{\boldsymbol{x}}$, and firing time instants thus determined, weighting functions acting on the relative error state and error control

remain to be appropriately selected. In harmony with the hybrid LQR scheme, the following quadratic functions are thus selected to weight, respectively, continuous evolution and instantaneous changes in the relative error state:

$$l_{ct}(\tilde{\boldsymbol{x}}) = \tilde{\boldsymbol{x}}^{\mathrm{T}}\boldsymbol{Q}_{ct}\tilde{\boldsymbol{x}}, \qquad l_{ds}(\tilde{\boldsymbol{x}}_k^-) = \tilde{\boldsymbol{x}}_k^{-\mathrm{T}}\boldsymbol{Q}_{ds}\tilde{\boldsymbol{x}}_k^-$$

where $\boldsymbol{Q}_{ct} = \boldsymbol{Q}_{ct}^{\mathrm{T}} \in \mathbb{R}^{n\times n} \geq \boldsymbol{0}$ and $\boldsymbol{Q}_{ds} = \boldsymbol{Q}_{ds}^{\mathrm{T}} \in \mathbb{R}^{n\times n} \geq \boldsymbol{0}$. Aiming to adjust the Hill-frame-related error variables acting on the deputy spacecraft, the following weighting matrices are therefore elected to provide a trade-off between the speed of response and the control effort in accordance with the control objectives, thereby obtaining satisfactory performance:

$$\boldsymbol{Q}_{ct} = diag(\,10\;\;10\;\;10\;\;10^3\;\;10^3\;\;10^3\,), \quad R_{ct} = 5\times 10^9$$
$$\boldsymbol{Q}_{ds} = diag(\,10\;\;10\;\;10\;\;10^3\;\;10^3\;\;10^3\,), \quad \boldsymbol{R}_{ds} = diag(\,5\times 10^8\;\;5\times 10^8\;\;5\times 10^8\,)$$

Preparatory to evaluating the performance of the hybrid feedback tracking controller in question, the initial conditions acting on the position and velocity vectors of the chief spacecraft, $\boldsymbol{r}_{c,in,0}$ and $\boldsymbol{v}_{c,in,0}$, respectively, are first determined by numerically solving Kepler's equation, given the initial orbital parameters of the chief spacecraft. Feeding $\mathcal{R}_{in-hl}$ and $\dot{\mathcal{R}}_{in-hl}$ with $\boldsymbol{r}_{c,in,0}$ and $\boldsymbol{v}_{c,in,0}$, the initial conditions on the deputy spacecraft, i.e., the initial conditions affecting the relative motion, are then obtained by:

$$\boldsymbol{r}_{d,in,0} = \boldsymbol{r}_{c,in,0} + \boldsymbol{\rho}_{in,0} = \boldsymbol{r}_{c,in,0} + \mathcal{R}_{in-hl}(\boldsymbol{r}_{c,in,0}, \boldsymbol{v}_{c,in,0})\boldsymbol{\rho}_{hl,0}$$
$$\boldsymbol{v}_{d,in,0} = \boldsymbol{v}_{c,in,0} + \dot{\boldsymbol{\rho}}_{in,0} = \boldsymbol{v}_{c,in,0} + \dot{\mathcal{R}}_{in-hl}(\boldsymbol{r}_{c,in,0}, \boldsymbol{v}_{c,in,0})\boldsymbol{\rho}_{hl,0} + \mathcal{R}_{in-hl}(\boldsymbol{r}_{c,in,0}, \boldsymbol{v}_{c,in,0})\dot{\boldsymbol{\rho}}_{hl,0}$$

Denoting the initial offset of the deputy spacecraft from the desired trajectory as $\left[\,\delta\boldsymbol{\rho}_{h,0}^{\mathrm{T}}\;\;\delta\dot{\boldsymbol{\rho}}_{h,0}^{\mathrm{T}}\,\right]^{\mathrm{T}}$, the initial relative coordinates expressed in the Hill-frame can be then set to:

$$\left[\,\boldsymbol{\rho}_{hl,0}^{\mathrm{T}}\;\;\dot{\boldsymbol{\rho}}_{hl,0}^{\mathrm{T}}\,\right]^{\mathrm{T}} = \boldsymbol{x}_{PCRO}(0) + \left[\,\delta\boldsymbol{\rho}_{hl,0}^{\mathrm{T}}\;\;\delta\dot{\boldsymbol{\rho}}_{hl,0}^{\mathrm{T}}\,\right]^{\mathrm{T}}$$

Therefore, the initial conditions acting on the *exact* equations of motion characterizing the coupled nonlinear dynamics of the chief and deputy spacecraft are given by $\left[\,\boldsymbol{r}_{c,in,0}^{\mathrm{T}}\;\;\boldsymbol{v}_{c,in,0}^{\mathrm{T}}\;\;\boldsymbol{r}_{d,in,0}^{\mathrm{T}}\;\;\boldsymbol{v}_{d,in,0}^{\mathrm{T}}\,\right]^{\mathrm{T}}$.

In order to evaluate the tracking performance of the proposed hybrid nonlinear optimal control architecture, a Lorentz-based LQR tracking controller is also designed and tested in this section, using an identical set of design parameters and initial conditions, by considering the linearized relative equations of motion with the following system and control input matrices:

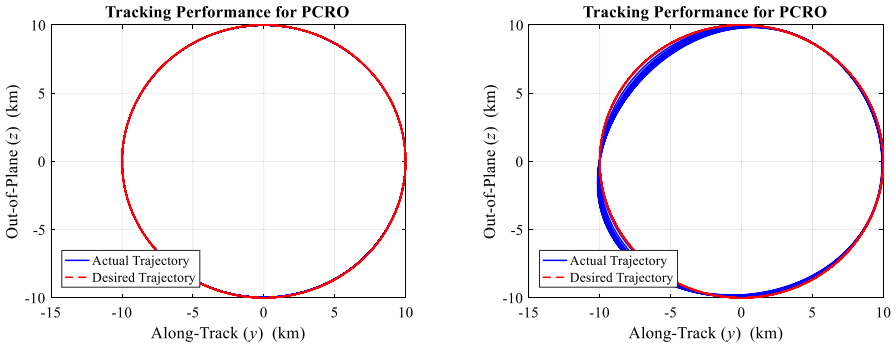

Fig. 4 Tracking performance for PCRO: hybrid nonlinear (left column) and Lorentz-based LQR (right column) control schemes for zero initial offset

$$\boldsymbol{A}_{ct}(t) = \boldsymbol{A}_{ct} = \begin{bmatrix} \boldsymbol{0}_{3\times3} & \boldsymbol{1}_{3\times3} \\ \begin{matrix} 3n_o^2 & 0 & 0 \\ 0 & 0 & 0 \\ 0 & 0 & -n_o^2 \end{matrix} & \begin{matrix} 0 & 2n_o & 0 \\ -2n_o & 0 & 0 \\ 0 & 0 & 0 \end{matrix} \end{bmatrix}$$

$$\boldsymbol{B}_{ct}(t) = \begin{bmatrix} \boldsymbol{0}_{3\times1} \\ \mathcal{R}_{in-hl}(\boldsymbol{r}_{c,in}, \boldsymbol{v}_{c,in})\left(\boldsymbol{v}_{c,in} - \boldsymbol{\omega}^{\times}_{\oplus,in}\boldsymbol{r}_{c,in}\right)^{\times}\boldsymbol{b}_{in}(\boldsymbol{r}_{c,in}) \end{bmatrix}$$

Furthermore, the following root-mean-square (RMS) norms are also defined and computed over 15 orbits to quantitatively assess the functionality of the proposed hybrid controller as opposed to the LQR control scheme:

$$\overline{\|\tilde{\boldsymbol{x}}_{hl}\|} = \sqrt{\frac{\int_0^{15\mathcal{T}} \tilde{\boldsymbol{x}}_{hl}^{\mathrm{T}}(t)\tilde{\boldsymbol{x}}_{hl}(t)\mathrm{d}t}{15\mathcal{T}}}\ (\mathrm{m}), \quad \overline{\left\|\dot{\tilde{\boldsymbol{x}}}_{hl}\right\|} = \sqrt{\frac{\int_0^{15\mathcal{T}} \dot{\tilde{\boldsymbol{x}}}_{hl}^{\mathrm{T}}(t)\dot{\tilde{\boldsymbol{x}}}_{hl}(t)\mathrm{d}t}{15\mathcal{T}}}\ (\mathrm{m/s})$$

$$\overline{\|\hat{q}\|} = \sqrt{\frac{\int_0^{15\mathcal{T}} \tilde{u}_{ct}^{*2}(t)\mathrm{d}t}{15\mathcal{T}}}\ (\mathrm{C/kg}), \quad \overline{\left\|\boldsymbol{f}_{imp}\right\|} = \sqrt{\frac{\sum_{k=1}^{\mathcal{K}} (\tilde{\boldsymbol{u}}_{ds,k}^{*\mathrm{T}}\tilde{\boldsymbol{u}}_{ds,k}^{*})}{\mathcal{K}}}\ (\mathrm{N\cdot s/kg})$$

wherein $\mathcal{T}$ defines the orbital period. In this regard, the RMS norms of relative position error, $\overline{\|\tilde{\boldsymbol{x}}_{hl}\|}$, and impulsive force, $\overline{\left\|\boldsymbol{f}_{imp}\right\|}$, can be used as important criteria for high precision and efficient fuel formation, respectively. By adjusting the size of the diagonal terms of the aforementioned weighting matrices, a trade-off between tracking error accuracy and fuel expenditure can be therefore balanced to achieve high precision formation with low fuel requirements.

In the first attempt, each feedback tracking controller experiences undemanding initial conditions with no initial offset, i.e., $\delta\boldsymbol{\rho}_{hl,0} = \delta\dot{\boldsymbol{\rho}}_{hl,0} = \boldsymbol{0}_{3\times1}$. The simulation results are shown in Figs. 4, 5, and 6 and Table 2. Figure 4 depicts the resultant tracking performance for both optimal controllers when the initial offset is zero. As is obvious, the linear Lorenz-based controller deviates slightly from the desired trajectory over the operating time even for these undemanding initial conditions. On the contrary, the control system equipped with a hybrid architecture tracks the

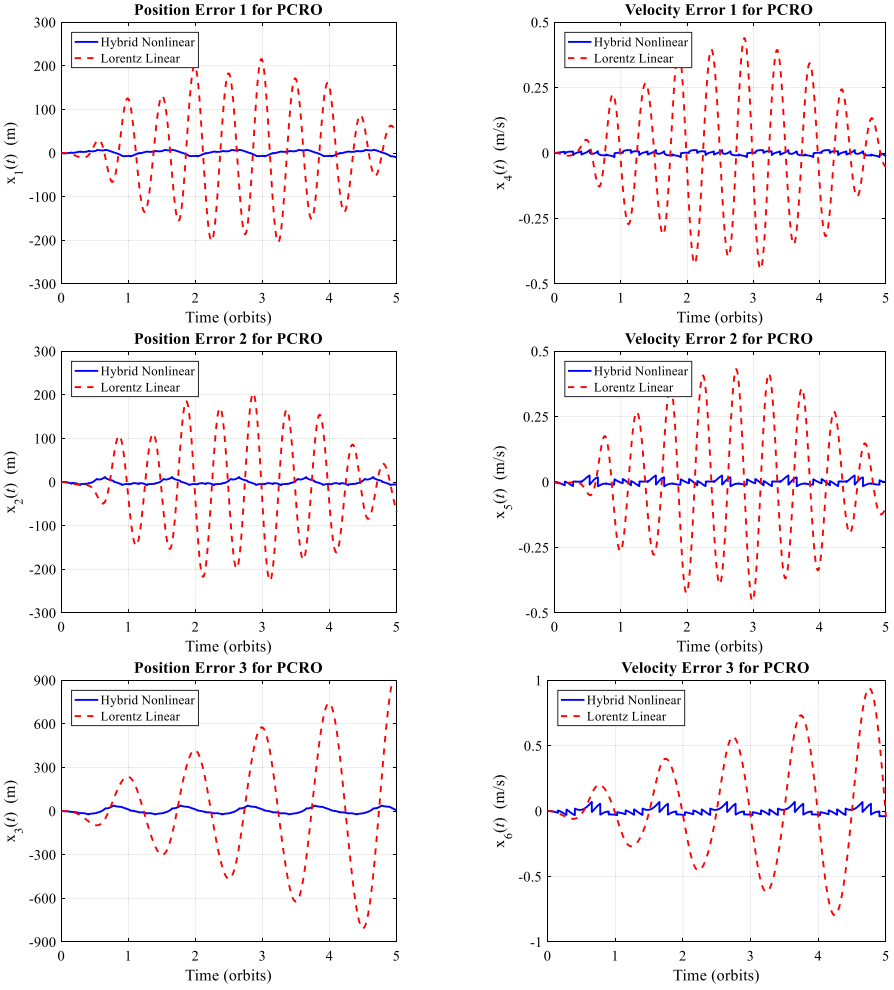

Fig. 5 Relative position (left column) and velocity (right column) errors over 5 orbits for hybrid nonlinear and Lorentz-based LQR control schemes with zero initial offset

PCRO trajectory perfectly. Furthermore, Fig. 5 illustrates how the relative state errors evolve over 5 orbits when each of the abovementioned optimal controllers is utilized. Whereas the relative position and velocity errors are insignificant for the hybrid control scheme, they are widely oscillating about the zero state errors in the x and y directions with unbounded growth in the z direction for the single-mode Lorentz-based controller. This obviously shows that the control system which only employs the Lorentz force as a means of actuation is uncontrollable in the z direction for this specific choice of inclination.

Shown in Fig. 6, the Lorentz (continuous-time) and impulsive control inputs are plotted. As can be seen, a noticeable reduction in the specific charge pertinent to the proposed hybrid control scheme is obvious as opposed to the LQR controller.

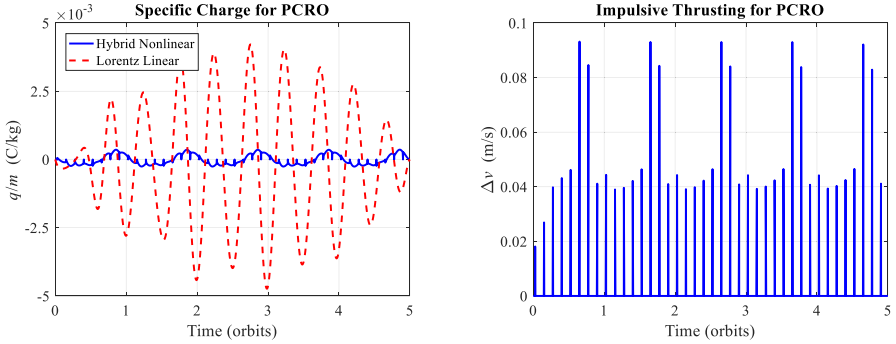

Fig. 6 Estimation of required electrostatic charge (left column) and impulsive thrusts (right column) for hybrid and Lorentz-based control schemes with zero initial offset

Table 2 Functional performance of hybrid nonlinear optimal control scheme in comparison to Lorentz-based LQR controller with zero initial offset

Parameters	$\mathcal{J}$	$\overline{\|\tilde{\boldsymbol{x}}_h\|}$ m	$\overline{\|\dot{\tilde{\boldsymbol{x}}}_h\|}$ m/s	$\overline{\|\hat{q}\|}$ C/kg	$\overline{\|\boldsymbol{f}_{imp}\|}$ N · s/kg
Hybrid nonlinear	5.56×10^{8}	1.96×10^{1}	2.66×10^{-2}	1.92×10^{-4}	5.72×10^{-2}
Lorentz linear	3.76×10^{11}	6.37×10^{2}	9.56×10^{-1}	5.62×10^{-3}	–
Improvement	99.85%	96.92%	97.22%	96.58%	–

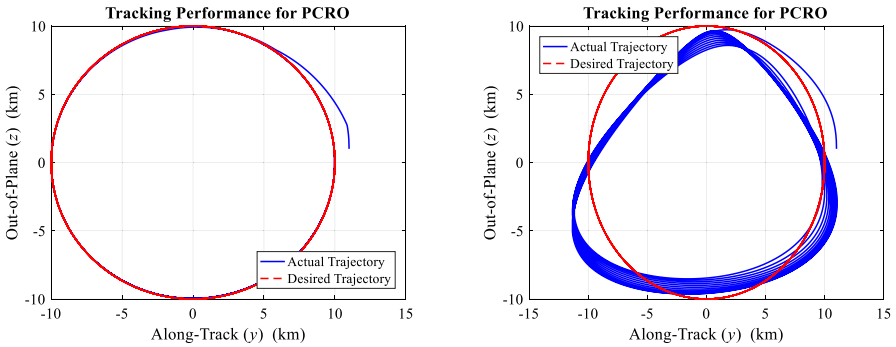

Fig. 7 Tracking performance for PCRO: hybrid nonlinear (left column) and Lorentz-based LQR (right column) control schemes for considerable nonzero initial offset from the desired trajectory

Summarized in Table 2, a quantitative assessment for the parameters characterizing the tracking performance of both controllers is presented. As can be observed, the quantities associated with the proposed hybrid control architecture are significantly enhanced as compared to the Lorentz-based LQR controller. For instance, the performance index and the specific charge experience, respectively, considerable improvement of 99.85 and 96.58 percent over 15 orbits.

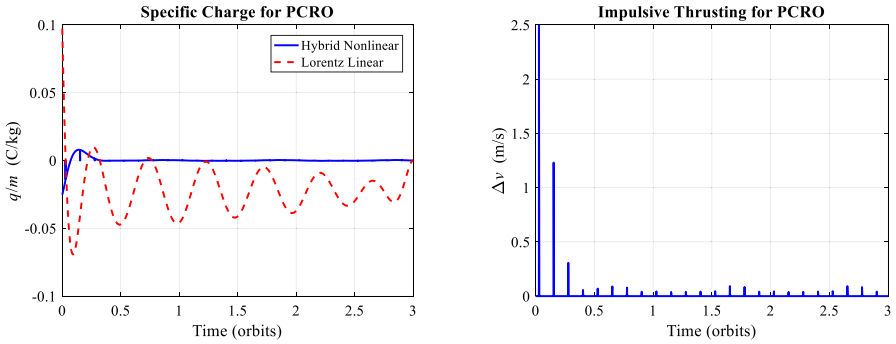

Fig. 8 Estimation of required electrostatic charge (left column) and impulsive thrusts (right column) for hybrid and Lorentz-based control schemes with nonzero initial offset

In the next attempt, the intended formation establishment is assumed to start with a considerable initial offset from the desired trajectory as follows:

$$\left[\,\delta\boldsymbol{\rho}_{h,0}^{\mathrm{T}}\;\;\delta\dot{\boldsymbol{\rho}}_{h,0}^{\mathrm{T}}\,\right]^{\mathrm{T}} = \left[\,1000\text{ m}\;\;1000\text{ m}\;\;1000\text{ m}\;\;0.1\text{ m/s}\;\;0.1\text{ m/s}\;\;0.1\;\;\text{m/s}\right]^{\mathrm{T}}$$

The simulation results exhibiting how the *exact* equations of relative motion react to the J_2-effect perturbations and the initial conditions involving nonzero initial offset are presented in Figs. 7, 8 and 9 and Table 3. Figure 7 shows the tracking performance of the hybrid and Lorentz-based controllers for a PCRO-based desired trajectory. As is apparent, the tracking performance for the hybrid control architecture is significantly improved as compared to the Lorentz-based controller. Whereas the hybrid controller perfectly tracks the desired trajectory, the Lorentz-based linear controller exhibits inferior performance, undergoing a considerable deviation from the desired PCRO over 15 orbits.

The evolution of the Lorentz (continuous-time) and impulsive control inputs are also plotted in Fig. 8, where a considerable reduction in the specific charge corresponding to the hybrid controller in contrast to the Lorentz-based scheme is obvious. Eliminating excessive load on Lorentz-based actuators, the feasibility of the Lorentz-augmented formation flight control system can be thus facilitated.

Furthermore, the time histories of relative position and velocity errors for both control frameworks in question are depicted in Fig. 9 over 3 orbits. As is evident, the relative state settles to the desired trajectory immediately after impulsive thrusts are collaboratively utilized with the Lorentz-based actuation, causing the state errors to converge to zero, which in consequence demonstrates satisfactory tracking performance of the proposed hybrid control architecture in terms of settling time and overshoot with relative state errors settling within one orbit. For the Lorentz-based controller, however, the relative state errors are still significantly large with a secular growth in the z direction due primarily to uncontrollability along this specific axis. This obviously justifies use of an auxiliary actuation mechanism for the Lorentz-augmented formation flight control system.

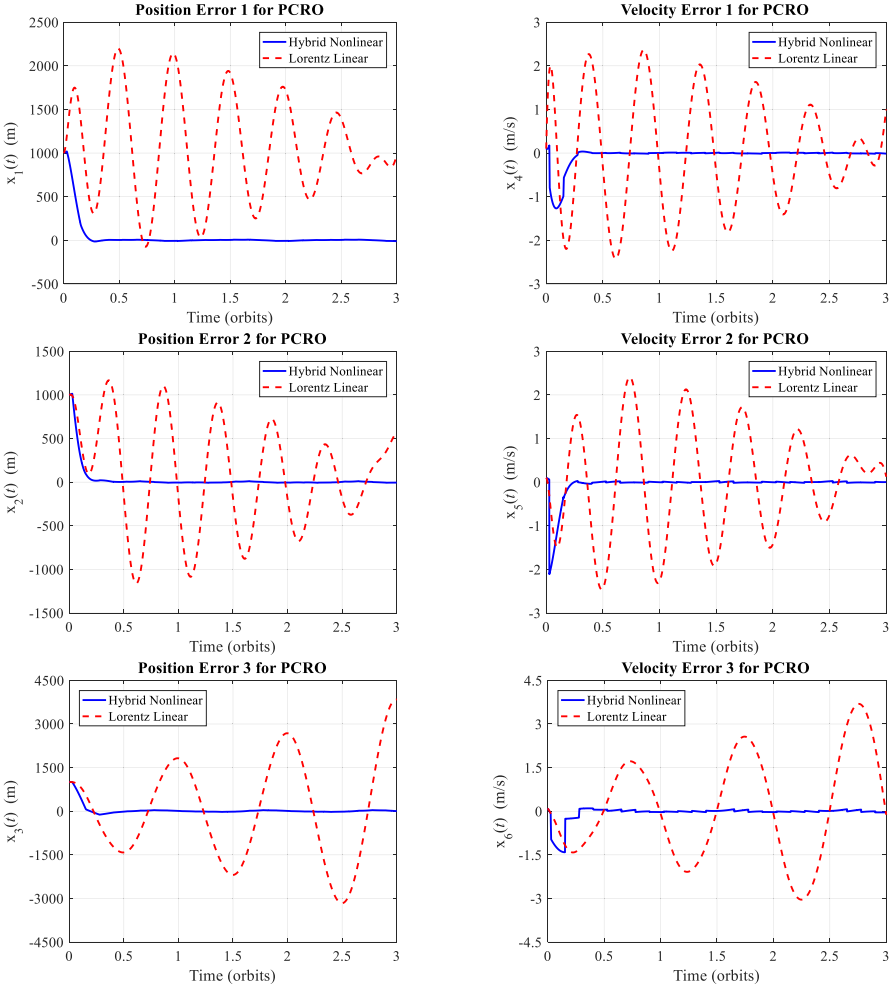

Fig. 9 Relative position (left column) and velocity (right column) errors over 3 orbits for hybrid nonlinear and Lorentz-based LQR control schemes with nonzero initial offset

Table 3 Functional performance of hybrid nonlinear optimal control scheme in comparison to Lorentz-based controller with nonzero initial offset

Parameters	$\mathcal{J}$	$\overline{\|\tilde{\boldsymbol{x}}_h\|}$ m	$\overline{\|\tilde{\dot{\boldsymbol{x}}}_h\|}$ m/s	$\overline{\|\hat{q}\|}$ C/kg	$\overline{\|\boldsymbol{f}_{imp}\|}$ N · s/kg
Hybrid nonlinear	1.83×10^{10}	1.23×10^{2}	2.04×10^{-1}	1.18×10^{-3}	2.62×10^{-1}
Lorentz linear	7.96×10^{12}	2.83×10^{3}	4.98×10^{0}	4.21×10^{-2}	–
Improvement	99.77%	95.65%	95.90%	97.19%	–

Summarized in Table 3, a quantitative assessment for the tracking performance of both hybrid and single-mode feedback controllers is presented. As is apparent,

the quantities associated with the hybrid nonlinear control synthesis are significantly improved in comparison with the Lorentz-based controller with, for instance, the performance index and the specific charge decreasing by 99.77 and 97.19 percent, respectively, over 15 orbits. Moreover, the feasibility of the proposed hybrid controller in terms of actively modulated charges is also demonstrated with a required specific charge on the order of 1.18×10^{-3} kg/C, which lies within the generally acceptable range proposed in [13, 14] as a near-term feasible value for LEOs.

6 Conclusion

In this paper, an optimal control design framework for hybrid nonlinear time-dependent dynamical systems involving an interacting amalgam of continuous-time and discrete-time dynamics has been developed. A hybrid computational framework involving two numerical schemes was proposed to solve the hybrid version of the Hamilton–Jacobi–Bellman (HJB) equation with time-dependency in an interacting manner. The resultant control design framework was then applied to spacecraft formation flying establishment under the action of the Lorentz force and impulsive thrusting. The outcome was a hybrid optimal pair of Lorentz and impulsive control inputs which alternated between continuous-time and discrete-time subsystems at an appropriate sequence of time instants to collaboratively maintain bounded relative motion between spacecraft in formation flight. As a consequence, not only were the uncontrollability issues pertinent inherently to the Lorentz-actuated control systems effectively resolved, but use of both continuous-time and impulsive control inputs was also optimized. Furthermore, the simulation results demonstrated the superiority of the proposed control architecture in terms of tracking performance and required control usage as compared to a Lorentz-based linear controller in addition to its feasibility in terms of actively modulated charges.

References

[1] Atchison, J.A., Peck, M.A.: Lorentz-augmented Jovian Orbit Insertion. J. Guid. Control. Dyn. **32**(2), 418–423 (2009). https://doi.org/10.2514/1.38406
[2] Atchison, J.A., Peck, M.A., Streetman, B.J.: Lorentz accelerations in the earth flyby anomaly. J. Guid. Control. Dyn. **33**(4), 1115–1122 (2010). https://doi.org/10.2514/1.47413
[3] Beard, R.: Improving the Closed-loop Performance of Nonlinear Systems. Ph.D. thesis, Rensselaer Polytechnic Institute, Troy, NY (1995)
[4] Beard, R., Saridis, G., Wen, J.: Galerkin approximations of the generalized Hamilton–Jacobi–Bellman Equation. Automatica **33**(12), 2159–2177 (1997)
[5] Beard, R., McLain, T.: Successive galerkin approximation algorithms for nonlinear optimal and robust control. Int. J. Control **71**(5), 717–743 (1998)
[6] Clohessy, W.H., Wiltshire, R.S.: Terminal guidance system for satellite rendezvous. J. Aerosp. Eng. **27**(9), 653–658 (1960). https://doi.org/10.2514/8.8704
[7] de Ruiter, A.H.J., Damaren, C.J., Forbes, J.R.: Spacecraft Dynamics and Control: An Introduction. Wiley, Hoboken (2013)
[8] Fletcher, C.A.J.: Computational Galerkin Methods. Springer Series in Computational Physics. Springer, New York (1984)

[9] Gangestad, J.W., Pollock, G.E., Longuski, J.M.: Propellantless stationkeeping at Enceladus via the electromagnetic Lorentz force. J. Guid. Control. Dyn. **32**(5), 1466–1475 (2009). https://doi.org/10.2514/1.42769
[10] Haddad, W.M., Chellaboina, V., Kablar, N.A.: Nonlinear impulsive dynamical systems. Part II: stability of feedback interconnections and optimality. Int. J. Control. **74**(17), 1659–1677 (2001). https://doi.org/10.1080/00207170110080959
[11] Huang, X., Yan, Y., Zhou, Y., Zhang, H.: Pseudospectral method for optimal propellantless Rendezvous using geomagnetic Lorentz force. Appl. Math. Mech. **36**, 609–618 (2015). https://doi.org/10.1007/s10483-015-1936-7
[12] Kong, E.M.C., Kwon, D.W., Schweighart, S.A., Elias, L.M., Sedwick, R.J., Miller, D.W.: Electromagnetic formation flight for multi-satellite arrays. J. Spacecr. Rocket. **41**(4), 659–666 (2004). https://doi.org/10.2514/1.2172
[13] Peck, M.A.: Prospects and challenges for Lorentz-augmented orbits. In: Proceedings of the AIAA guidance, navigation, and control conference, San Francisco, CA, (2005). https://doi.org/10.2514/6.2005-5995
[14] Peck, M.A., Streetman, B.J., Saaj, C.M., Lappas, V.: Spacecraft formation flying using Lorentz forces. J. Br. Interpl. Soc. **60**, 263–267 (2007)
[15] Pollock, G.E., Gangestad, J.W., Longuski, J.M.: Inclination change in low-earth orbit via the geomagnetic Lorentz force. J. Guid. Control. Dyn. **33**(5), 1387–1395 (2010). https://doi.org/10.2514/1.48610
[16] Pollock, G.E., Gangestad, J.W., Longuski, J.M.: Analytical solutions for the relative motion of spacecraft subject to Lorentz-force perturbations. Acta Astronaut. **68**, 204–217 (2011). https://doi.org/10.1016/j.actaastro.2010.07.007
[17] Quarteroni, A., Sacco, R., Saleri, F.: Numerical Mathematics. Springer, New York (2000)
[18] Sharifi, E., Damaren, C.J.: A numerical approach to hybrid nonlinear optimal control. Int. J. Control. (2020). https://doi.org/10.1080/00207179.2020.1763471
[19] Sobiesiak, L.A., Damaren, C.J.: Optimal continuous/impulsive control for Lorentz-augmented spacecraft formations. J. Guid. Control. Dyn. **38**(1), 151–157 (2015). https://doi.org/10.2514/1.G000334
[20] Sobiesiak, L.A., Damaren, C.J.: Impulsive spacecraft formation maneuvers with optimal firing times. J. Guid. Control. Dyn. **38**(10), 1994–1999 (2015). https://doi.org/10.2514/1.G001095
[21] Sobiesiak, L.A., Damaren, C.J.: Lorentz-augmented spacecraft formation reconfiguration. IEEE Trans. Control Syst. Technol. **24**(2), 514–524 (2016). https://doi.org/10.1109/TCST.2015.2461593
[22] Streetman, B.J., Peck, M.A.: Synchronous orbits and disturbance rejection using the geomagnetic Lorentz force. In: Proceedings of AIAA guidance, navigation, and control conference, keystone, CO (2006)
[23] Streetman, B.J., Peck, M.A.: New synchronous orbits using the geomagnetic Lorentz force. J. Guid. Control. Dyn. **30**(6), 1677–1690 (2007). https://doi.org/10.2514/1.29080
[24] Streetman, B.J.: Lorentz-augmented Orbit Dynamics and Mission Design. Ph.D. Thesis, Cornell University, Ithaca, NY, (2008).
[25] Streetman, B.J., Peck, M.A.: Gravity-assist Maneuvers augmented by the Lorentz force. J. Guid. Control. Dyn. **32**(5), 1639–1647 (2009). https://doi.org/10.2514/1.35676
[26] Terrestrial Planet Finder: Origins of Stars, Planets, and Life. Jet Propulsion Laboratory (JPL), California Institute of Technology, Pasadena, CA, (1999)
[27] Vadali, S.R., Schaub, H., Alfriend, K.T.: Initial conditions and fuel-optimal control for formation flying of satellites. In: Proceedings of the AIAA guidance, navigation, and control conference and exhibit, Portland, OR (1999). https://doi.org/10.2514/6.1999-4265
[28] Vaddi, S.S., Vadali, S.R., Alfriend, K.T.: Formation flying: accommodating nonlinearity and eccentricity perturbations. J. Guid. Control. Dyn. **26**(2), 214–223 (2003)
[29] Yamakawa, H., Yano, K., Bando, M., Tsujii, S.: Spacecraft relative dynamics under the influence of geomagnetic Lorentz force. In: Proceedings of AIAA/AAS astrodynamics specialist conference, Toronto, ON, (2010)